

Properties of Galactic Dark Matter: Constraints from Astronomical Observations

B. Burch and R. Cowsik

(Dated: December 3, 2024)

Abstract

The distributions of normal matter, like stars and gas, and of dark matter in the Galaxy are coupled to each other as they both move in the common gravitational potential that receives contributions from the density distributions of both these components. In order to fully exploit this interplay and to derive the various properties of dark matter relevant to their direct and indirect detection, we have comprehensively reviewed the astronomical observations of the components of normal matter, both in regard to their spatial and velocity distributions. We then postulate that the phase-space distribution of dark matter follows a lowered-isothermal form, and we solve, self-consistently, the Poisson equation to construct several models for the spatial and velocity distributions of dark matter. In this paper, we compute the total gravitational potential of the normal and dark matter components in these models and investigate their consistency with current observations of the rotation curve of the Galaxy and of the spatial and velocity distributions of blue horizontal-branch and blue straggler stars. Even with this demand of consistency, there still remains a large number of models with a range of parameters characterizing the distribution of dark matter:

- i. the dark matter density at the Galactic center, $\rho_{DM0} = 250 - 500 \text{ GeV/cm}^3$,
- ii. the dark matter density at the location of the Solar system, $\rho_{DM}(R_\odot) = 0.47 - 0.76 \text{ GeV/cm}^3$,
- iii. the root-mean-square speed of the dark matter particles at the location of the Solar system, $\langle v_{DM}^2(R_\odot) \rangle^{1/2} = 480 - 515 \text{ km/s}$.
- iv. The best choice of parameters, within the range of allowed values, for the surface density of the disk $\Sigma_{d,\odot} = 55 \text{ M}_\odot/\text{pc}^2$, are the following: $\rho_{DM0} \approx 500 \text{ GeV/cm}^3$, $\rho_{DM}(R_\odot) \approx 0.66 \text{ GeV/cm}^3$ and $\langle v_{DM}^2(R_\odot) \rangle^{1/2} \approx 490 \text{ km/s}$.

After presenting these results, we proceed to discuss possible astronomical observations that may further limit the range of the allowed models. The predictions of the allowed models for direct and indirect detection will be discussed separately in a companion paper.

I. INTRODUCTION

Though the precise phase-space distribution of Galactic dark matter is still unknown, much effort has been invested in understanding the distribution and dynamics of dark matter

in the Milky Way for the purposes of understanding the overall dynamics and structure of our Galaxy as well as for the planning and interpretation of their direct and indirect detection. Most studies assume the framework of the Standard Halo Model of dark matter, which envisages the Milky Way as embedded in an isothermal dark matter halo described by a Maxwell-Boltzmann phase-space distribution with a local dark matter density of 0.3 GeV/cm^3 (Many studies that have been reported in the literature find a local dark matter density in the wider range of $0.2\text{-}0.6 \text{ GeV/cm}^3$ [1–5].) and a velocity dispersion of 270 km/s , and the radial distribution of its density is truncated at the “virial radius” to keep the mass of the halo and the escape velocity finite. However, it is well understood that a Maxwellian distribution does not properly describe Galactic dark matter [6] as it leads to infinite extent and total mass for the system. In this paper, we aim to improve on the constraints on the phase-space distribution of Galactic dark matter, and in the process, derive the density distribution and other properties pertaining to Galactic dark matter particles, using a more appropriate phase-space distribution.

The basic strategy for probing the phase-space distribution (PSD) of dark matter is well established [9]. The distributions of dark matter and visible matter are coupled to each other as they are both influenced by the gravitational potential of the Galaxy, to which each of these makes its own contribution. Thus, when we have at hand the density distribution of visible matter, determined by astronomical observations, it is a straight-forward matter to calculate the gravitational potential generated by visible matter. Then, for any assumed functional form for the PSD of dark matter, given a set of parameters, we can solve the non-linear Poisson equation to determine the potential contributed by dark matter. Thus, having determined the total potential of the Galaxy, we may then use astronomical probes like the rotation curve of the Galaxy and the velocity and spatial distribution of stars to fix the values of the parameters characterizing the PSD function of dark matter that provide good fit to these observations.

In order to constrain the phase-space distribution of Galactic dark matter better than in earlier analyses, observations of the distribution of the various visible mass components of the Milky Way are reviewed in detail, and a simple axisymmetric model of the density distribution of the Galactic stars and gas is constructed. The particles of dark matter move in the gravitational potential generated by the visible matter and by their own mass distribution, and their spatial distribution is cut off at the “virial radius” defined as “the radius

of a sphere centred on the halo centre which has an average density of Δ times the critical density, but the definition of Δ varies between authors” [7] from $\Delta = 200$ [7] to $\Delta = 355$ [8] or more. Assuming a lowered-isothermal phase-space distribution for Galactic dark matter, the gravitational potential from dark matter is computed from iterative, self-consistent, solutions of Poisson’s equation, following a method suggested by Cowsik, Ratnam, and Bhattacharjee [9]. In this way, many dark matter profiles are generated with a wide range of properties depending on the specific choice of the parameters of their PSD. These models are then compared in turn with the current observations of the Galactic rotation curve and to recent observations of the velocity and spatial distribution of blue horizontal-branch (BHB) and blue straggler (BS) stars in the outer Galaxy. Comparing the dark matter models with the rotation curve and with the BHB/BS distributions separately allows for a wide range of dark matter properties. On the other hand, when we demand that the models fit both these simultaneously for the same choice of parameters, the parameter space narrows down and becomes almost exclusively dependent on the value chosen for the surface density of the visible disk of the Galaxy. However, even in the combined analysis of the rotation curve and the stellar distributions, a significant range of parameters for the phase-space distribution of dark matter is still allowed. Within the current estimates of the mass of the Galactic disk, we find that the best estimates for the local dark matter density are $0.47\text{--}0.76 \text{ GeV}/\text{cm}^3$ with the value at the Galactic center ranging from $250\text{--}500 \text{ GeV}/\text{cm}^3$. The escape speed from the center of the Galaxy lies in the range $\sim 940 - 980 \text{ km/s}$ and the root-mean-square speed of dark matter particles in the Solar neighborhood is found to be $\sim 480\text{--}515 \text{ km/s}$ for the most favored models.

II. THE VISIBLE MATTER DISTRIBUTION

In order to derive the Galactic dark matter distribution, the distribution of visible matter in the Galaxy must be well understood, as it is their interplay that allows us to probe the dark matter. We have completed an extensive survey of the current observations of the distributions of stars and gas in the Milky Way and constructed a simple axisymmetric model of the Galaxy that agrees with current data. The known mass distribution of the Galaxy derives contributions from the central black hole, central bulge, disk, and stellar halo populations. In this analysis, the stellar halo is neglected because its contribution to

the visible matter density is on the order of 0.1% at R_\odot , the distance from the Sun to the Galactic center [10], and it is therefore expected to contribute negligibly to the dynamics of the Galaxy. Likewise, the black hole and nuclear bulge, whilst playing important roles very close to the Galactic center, contribute negligibly to the overall dynamics of the Galaxy in the regions of interest. For the purposes of computing the gravitational potential in this paper, the visible Galaxy consists of a central bulge and a thin and a thick exponential disk. There are several ways to model these components, and here, models that most closely fit the observations of the stars and gas are adopted.

A. The Disk

The mass density of both the thin (tn) and the thick (tk) disk components are typically modeled as double-exponential functions with early evidence for their validity given by Freeman [11]. Following the notation used in many recent analyses [7, 12], the densities for the separate components may be written as,

$$\rho_{tn}(r, z) = \frac{\Sigma_{tn,0}}{2z_{tn}} e^{-z/z_{tn}} e^{-r/r_{tn}}, \quad (1)$$

$$\rho_{tk}(r, z) = \frac{\Sigma_{tk,0}}{2z_{tk}} e^{-z/z_{tk}} e^{-r/r_{tk}}, \quad (2)$$

$$\rho_d = \rho_{tn} + \rho_{tk}, \quad (3)$$

$$\Sigma_d = \Sigma_{tn} + \Sigma_{tk}, \quad (4)$$

in cylindrical coordinates, where ρ_d is the total density of the Galactic disk, $\Sigma_{tk/tn,0}$ are the surface densities near the Galactic Center (including both stars and gas), $z_{tk/tn}$ are the scale heights, and $r_{tk/tn}$ are the radial scale lengths for the thick and thin components respectively. The masses of the two components are given by

$$M_{tk/tn} = 2\pi \Sigma_{tk/tn,0} r_{tk/tn}^2. \quad (5)$$

For the total local surface density at R_\odot from visible matter, we consider the range

$$\Sigma_{d,\odot} = 40 - 70 \text{ } M_\odot \text{pc}^{-2},$$

which is the range found in the literature [13–21]. For convenience, the ratio of the thick disk surface density at R_\odot to the total surface density at R_\odot is taken to be

$$\frac{\Sigma_{tk,\odot}}{\Sigma_{tk,\odot} + \Sigma_{tn,\odot}} = 0.1, \quad (6)$$

a value that is also within the range of the findings of many studies [22–30]. The choice of the ratio in eq. 6, within observational constraints, does not have a significant effect on the rotation curve or other dynamical indicators calculated in this paper.

The radial scale lengths r_{tn} and r_{tk} are chosen from the compilation of observations to be 3 kpc and 3.5 kpc respectively. The scale heights are chosen to be $z_{tn} = 350$ pc and $z_{tk} = 900$ pc, close to the values determined by Jurić *et al.* [31] and are seen to not have a strong effect on the calculated rotation curve, agreeing with the analysis of McMillan [7]. The above parameters yield a combined disk mass in the range $3.57 - 6.24 \times 10^{10} M_{\odot}$. We show the mass profiles of the Galactic disk and bulge in Fig. 1. Note, this simple disk model does not include some of the finer structures of the disk such as the spiral arms or the warp included in other analyses [32] since an axisymmetric model is adequate to describe the overall dynamics and accords computational simplicity.

The disk potential has the form [13, 33]

$$\begin{aligned} \Phi_d(r, z) = -2\pi G \bigg(& \Sigma_{tn,0} r_{tn}^2 \int_0^\infty dk \frac{J_0(kr)}{[1 + (kr_{tn})^2]^{3/2}} \frac{e^{-k|z|} - (kz_{tn})e^{-|z|/z_{tn}}}{1 - (kz_{tn})^2} \\ & + \Sigma_{tk,0} r_{tk}^2 \int_0^\infty dk \frac{J_0(kr)}{[1 + (kr_{tk})^2]^{3/2}} \frac{e^{-k|z|} - (kz_{tk})e^{-|z|/z_{tk}}}{1 - (kz_{tk})^2} \bigg). \end{aligned} \quad (7)$$

Note the potential includes integration over Bessel functions, which slows down numerical calculations of the rotation curve for the different models. We find that using an adaptive quasi-Monte Carlo method in *Mathematica* provides the quickest computation time without sacrificing accuracy.

Since there are some uncertainties in the values of $\Sigma_{tk,0}$ and $\Sigma_{tn,0}$, we also consider, for completeness, a maximal disk model where the density of the disk is increased to its maximal value without exceeding the rotation speed anywhere within the Solar circle. After including the standard parameters of the bulge at the Galactic center, we increase arbitrarily the surface densities of the disk components to significantly larger values that lie outside most observational constraints. We find that a surface density up to $\Sigma_{d,\odot} = 100 M_{\odot} \text{ pc}^{-2}$ is not inconsistent with the rotation curve up to ~ 6 kpc, as shown in Fig. 2.

B. The Bulge

The bulge, in cylindrical coordinates, is described by a Plummer density profile of the form

$$\rho_b = \frac{3M_b}{4\pi b^3} \left(1 + \frac{r^2 + z^2}{b^2} \right)^{-5/2}, \quad (8)$$

where M_b is the total mass of the bulge and b is the scale radius. To determine M_b and b , we assume the dark matter contribution to the dynamics from $\sim 0.1 - 1$ kpc is small (an assumption that is justified *post facto*) and subtract only the disk contribution from the inner 1 kpc of the squared rotation curve. The resulting points are fit with the rotation curve derived from the Plummer density. The bulge parameters are found to be $M_b = 1.02 \times 10^{10} M_\odot$ and $b = 0.258$ kpc. The potential of the Plummer model has the simple analytical form

$$\Phi_b = -\frac{GM_b}{(r^2 + z^2 + b^2)^{1/2}} \quad (9)$$

and a velocity dispersion [34] given by

$$\sigma_b^2 = \frac{GM_b}{6(r^2 + z^2 + b^2)^{1/2}}. \quad (10)$$

We show the velocity dispersion in Fig. 3, along with measurements of the K and M bulge giants [35–37]. Note that the dispersion expected from the Plummer model agrees well with the observations, implying that this region is adequately described by a bulge-dominated density profile. Including the mass contribution from the disk in the bulge region does not noticeably change the velocity dispersion. A contour plot of the total visible density from both the bulge and disk components is shown in Fig. 4 for the $\Sigma_{d,\odot} = 700 M_\odot \text{ pc}^{-2}$ disk.

III. DYNAMICAL OBSERVATIONS: THE ROTATION CURVE AND STELLAR VELOCITY DISTRIBUTIONS

Recent observations of stars, interstellar gas, and masers have been able to extend our understanding of the dynamics of the Galaxy beyond the Solar circle as well as improving observations near the Solar location. The density and dynamics of these objects probe the Galactic gravitational potential. The gravitational potential in the Galactic plane as a function of the distance from the Galactic center can be determined from the rotational

speed of the Galaxy in the usual way:

$$\frac{v_c^2}{r} = \frac{\partial \Phi_{tot}}{\partial r}, \quad (11)$$

where Φ_{total} includes contributions from both the visible and dark matter components of the Galaxy. The best observations of the Milky Way’s rotation curve now span $\sim 1 - 20$ kpc. The Galactic potential can be probed up to ~ 90 kpc by considering the velocity distribution of BHB and BS stars. Recent compilations of carefully selected BHB stars by Xue *et al.* [38] and BHB and BS stars by Brown *et al.* [39] are used below to constrain the Galactic dark matter distribution.

A. The Rotation Curve

The best estimates of the gravitational potential in the Galactic plane within ~ 10 kpc of the Galactic center come from measurements of the Galactic rotation speed. We have compiled a large sample of the available observations [40–52], excluding only those with exceptionally high dispersion in the data [53]. The rotation curve inside the solar circle is well-determined by observations of HI regions and CO emission associated with HII regions. Outside the solar circle, distances to objects are much more difficult to accurately measure, so the errors in the rotation curve are correspondingly larger. We present a compilation of the data used in our analysis in Fig. 5, with error bars when available, along with a shaded band, which includes 2/3 of the data points in 1 kpc radial bins.

The Milky Way’s rotation curve is derived from line-of-sight observations of gas complexes, masers, planetary nebula, and other astrophysical objects. The calculation of the rotation speed is a function of R_\odot , the distance from the Galactic center to the Sun and Θ_\odot , the rotation speed of the Sun about the Galactic center. Recently, maser observations and measurements of stellar orbits near SgrA* have been able to constrain $R_\odot = 7.2 - 9$ kpc [55–59]. A summary of some estimates of R_\odot can be found in Avedisova [54]. We choose $R_\odot = 8.3$ kpc based on these and other stellar observations from the past decade. The ratio Θ_\odot/R_\odot is well constrained from masers and stellar orbits [57, 59, 60] and is in the range of $\Theta_\odot/R_\odot = 28.5 - 30.3$ km/s kpc $^{-1}$. We take $\Theta_\odot/R_\odot \approx 28.9$ km/s kpc $^{-1}$ such that $\Theta_\odot = 240$ km/s. This value of Θ_\odot differs significantly from the IAU standard values (see McMillan and Binney [61] and the references therein) of $R_\odot = 8.5$ kpc and $\Theta_\odot = 220$ km/s,

which gives $\Theta_{\odot}/R_{\odot} \approx 25.9 \text{ km/s kpc}^{-1}$, disagreeing with maser and stellar orbit observations. The result of reanalyzing the observations using the larger value of Θ_{\odot} is that the rotation curve gently rises from $\sim 2 - 15 \text{ kpc}$ instead of remaining flat. We have also made efforts to correct all the rotation curve data for new measurements of the peculiar motion of the sun $(U_{\odot}, V_{\odot}, W_{\odot})$, where V_{\odot} has been updated from $\sim 5 \text{ km/s}$ to $\sim 11 - 15 \text{ km/s}$ [61, 62]. We take $(U_{\odot}, V_{\odot}, W_{\odot}) = (11, 12, 7.5) \text{ km/s}$.

B. Blue Horizontal-Branch Stars

Xue *et al.* [38] have compiled an extensive list of the line-of-sight velocities of 2401 BHB stars from the Sloan Digital Sky Survey DR6 taking care to ensure their sample is pure and contains accurate data on both the distance and line-of-sight velocity of each star. They use this data to constrain cosmological simulations and estimate the virial mass of the Galaxy as well as derive the rotation curve up to $\sim 60 \text{ kpc}$. We combine their compilation of 2401 BHB stars within 60 kpc of the Galactic center with their separate compilation of stars at galactocentric distances of $\sim 60 - 90 \text{ kpc}$. This combined compilation extends from 5-90 kpc with line-of-sight velocities spanning $\pm 350 \text{ km/s}$. After rescaling the galactocentric distances and line-of-sight velocities for each star to correspond to the values of R_{\odot} and Θ_{\odot} chosen above, the observations are divided into eleven radial bins as seen in Figs. 6-8 where the velocity distribution is shown after averaging the positive and negative velocity distributions together in 50 km/s bins. Error bars are shown as $\pm\sqrt{N}$ where N is the average number of stars in each velocity bin.

Brown *et al.* have compiled a sample of 910 BHB and BS stars from the Hypervelocity Star Survey, which contains twice as many stars at $r \geq 50 \text{ kpc}$ compared to the compilations by Xue *et al.*, and they derive the velocity dispersion profile of the Milky Way out to $\sim 95 \text{ kpc}$. While the Brown *et al.* sample is complete in color, magnitude depth, and spatial coverage, there is some ambiguity in distinguishing BHB from BS stars. To achieve the ratio of BHB to BS stars as stated in Brown *et al.*, stars with $f_{BHB} \geq 0.6$ were taken to be BHB stars, where f is the likelihood of a candidate star being a BHB star as reported in Table 1 of Brown *et al.*, and any star with $f_{BHB} < 0.6$ was considered to be a BS star. This reproduces the 74% to 26% BHB to BS ratio in Brown *et al.* As with the stars in the compilation by Xue *et al.*, this sample too was rescaled for our adopted values of R_{\odot} and Θ_{\odot} .

We find that we are unable to reproduce the R_{BHB} and R_{BS} distances in Table 1 of Brown *et al.* for their choice of R_\odot , Θ_\odot and $(U_\odot, V_\odot, W_\odot)$. We calculate the heliocentric distance for the BHB and BS stars using eq. 2 in Brown *et al.* and convert it to a galactocentric distance in the usual way (see eq. 4 in Xue *et al.* [38]). The stellar observations are then divided into eight radial bins. The line-of-sight velocities are averaged and the error bars are determined in the same manner as for the Xue *et al.* distribution (see Figs. 9-11).

IV. THE GALACTIC DARK MATTER DISTRIBUTION

The phase-space distribution of Galactic dark matter is currently unknown. The density distribution of dark matter is controlled by the velocity distribution of the dark matter particles and the total gravitational potential Φ_{tot} in which they reside. The total potential receives contributions from the density distributions of both the visible and the dark matter components of the Galaxy:

$$\Phi_{tot} = \Phi_b + \Phi_d + \Phi_{DM}, \quad (12)$$

where Φ_b , Φ_d , and Φ_{DM} are the potentials contributed by the bulge, the disk, and the dark matter. In order to develop a self-consistent model for the dark matter in our Galaxy, we require a dynamical model whose phase-space distribution function represents a collisionless system that can be parameterized by the dark matter velocity dispersion, density at either the Galactic center or at R_\odot , and the size of the dark matter halo. A lowered isothermal (King) distribution, which is well described in Binney and Tremaine [63], and unlike the isothermal sphere, has a finite mass and non-singular central density, meets these requirements. Reasons for choosing the King distribution are also discussed in earlier papers [64, 65].

The distribution function of the King model is given by

$$f_K(\varepsilon) = \begin{cases} \frac{\rho_1}{(2\pi\sigma_{DM}^2)^{3/2}} \left(e^{\varepsilon/\sigma_{DM}^2} - 1 \right) & \text{for } \varepsilon > 0 \\ 0 & \text{for } \varepsilon \leq 0 \end{cases} \quad (13)$$

where

$$\varepsilon \equiv \Phi_0 - \left(\frac{1}{2} v^2 + \Phi_{tot} \right). \quad (14)$$

Φ_0 is the total potential at $r = 0$, and ρ_1 and σ are parameters that are related but not equal to the central dark matter density ρ_{DM0} and the dark matter velocity dispersion, which can

be directly calculated from the distribution function.

The dark matter density distribution is readily calculated by integrating the distribution function

$$\rho_{DM} = \int f_K d^3v \quad (15)$$

and vanishes at $r = r_t$ where $\varepsilon = 0$. For a known total potential, eq. 15 becomes

$$\begin{aligned} \rho_{DM}(\Psi(r, z)) &= \frac{\rho_1}{(2\pi\sigma_{DM}^2)^{3/2}} \int_0^{\sqrt{2\Psi(r, z)}} dv v^2 \left[\exp\left(\frac{\Psi(r, z) - \frac{1}{2}v^2}{\sigma_{DM}^2}\right) - 1 \right] \\ &= \rho_1 \left[e^{\Psi(r, z)/\sigma_{DM}^2} \operatorname{erf}\left(\frac{\sqrt{\Psi(r, z)}}{\sigma_{DM}}\right) - \sqrt{\frac{4\Psi(r, z)}{\pi\sigma_{DM}}} \left(1 + \frac{2\Psi(r, z)}{3\sigma_{DM}^2}\right) \right], \end{aligned} \quad (16)$$

where $\Psi(r, z)$ is the scaled potential at the position (r, z) , defined by

$$\Psi(r, z) \equiv \Phi_0 - \Phi_{tot}(r, z), \quad (17)$$

and $\sqrt{2\Psi(r, z)}$ is the Galactic escape speed from the location (r, z) .

Keeping in mind that ρ_{DM} , which is the source for Φ_{DM} , depends on Φ_{DM} itself, the dark matter potential has to be calculated iteratively by numerically solving the Poisson equation,

$$\nabla^2 \Phi_{DM}(r, z) = 4\pi G \rho_{DM}(r, z). \quad (18)$$

The procedure that we adopt here is a Legendre polynomial expansion as described in Cowsik *et al.* [9], which is based on the earlier work by Wilson [66] and Prendergast and Tomer [67]. In this way, we produce the density and gravitational potential for visible matter and dark matter separately as well as for the sum of the two components.

For the above calculations, we formulate the King distribution in terms of σ_{DM} , ρ_{DM0} , and Ψ_0/σ_{DM}^2 instead of ρ_1 and Φ_0 . The precise choices for σ , ρ_{DM0} , and Ψ_0/σ_{DM}^2 are made by solving eq. 18 for a range of values, calculating the corresponding rotation curve (eq. 19), and comparing the results to the observations of the rotation curve and to the velocity distribution of BHB and BS stars.

V. COMPARISON WITH ASTRONOMICAL OBSERVATIONS

In order to compare with the rotation curve and the BHB and BS observations, a large sample of possible dark matter models were generated, encompassing $\rho_{DM0} \approx 1 - 1000$

GeV/cm³, $\sigma_{DM} \approx 100 - 1000$ km/s, and $\Psi_0/\sigma_{DM}^2 \approx 1 - 25$ for each of the light, heavy, and maximal disks. For each model, $\Psi(r, z)$, ρ_{DM0} , $< v_{DM}^2(R_\odot) >^{1/2}$, $v_c(r)$, the escape velocity, and the King radius were calculated. In Figs. 12-15 we show as examples contour plots of the total Galactic potential and the dark matter density in the Galaxy for the choice $\Sigma_{d,\odot} = 70 \text{ M}_\odot/\text{pc}^2$, $\rho_{DM0} = 500 \text{ GeV/cm}^3$, and $\sigma_{DM}=200 \text{ km/s}$.

A. Comparison with the Rotation Curve

The very discovery of dark matter in the Galaxy and the subsequent determinations of its characteristics rest almost exclusively on the measurements of the rotation curve. In this section, we will compare the sequence of models that we have calculated with our compilation of observations shown in Fig. 2 to limit the range of parameters characterizing the phase-space distribution function of dark matter. The theoretical estimates of the rotational velocities are calculated using the expression

$$v_c(r) = \left(r \frac{\partial \Phi_{tot}(r, 0)}{\partial r} \right)^{1/2} = \left(r \frac{\partial}{\partial r} [\Phi_b(r, 0) + \Phi_d(r, 0) + \Phi_{DM}(r, 0)] \right)^{1/2} \quad (19)$$

for three sets of models characterized by the three choices of $\Sigma_{d,\odot}$, $40 \text{ M}_\odot \text{ pc}^{-2}$, $70 \text{ M}_\odot \text{ pc}^{-2}$, and $100 \text{ M}_\odot \text{ pc}^{-2}$, which are displayed in Figs. 16-18 respectively. The full range of density profiles for these models are shown in Figs. 19-21. All the characteristics of the dark matter distribution for each of the models in these three sets is also presented in Tables I-III. All the models displayed here satisfy the criterion that $v_c(r = R_\odot)$ lies in the range 220-260 km/s, which encompasses 2/3 of all the available measurements.

The following points may be noted after a perusal of the figures and tables:

1. All these models provide good fits to the observed rotation curve within the solar circle ($r < R_\odot$).
2. The larger the assumed value of the surface density of the disk, larger is the range of allowed parameters of the dark matter distributions.
3. Setting aside the maximal disk as too far outside the observed values and focusing attention on the $\Sigma_{d,\odot} = 40 \text{ M}_\odot \text{ pc}^{-2}$ and $\Sigma_{d,\odot} = 70 \text{ M}_\odot \text{ pc}^{-2}$ disks, which may span the realistic possibilities, still leaves a considerable range in the parameters:

- (a) $848.8 \text{ km/s} \leq v_{esc}(0) \leq 1010.0 \text{ km/s}$
- (b) $516.0 \text{ km/s} \leq v_{esc}(R_\odot) \leq 739.7 \text{ km/s}$
- (c) $25 \text{ GeV/cm}^3 \leq \rho_{DM0} \leq 500 \text{ GeV/cm}^3$
- (d) $0.164 \text{ GeV/cm}^3 \leq \rho_{DM}(R_\odot) \leq 0.853 \text{ GeV/cm}^3$
- (e) $400 \text{ km/s} \leq \langle v_{DM}^2(R_\odot) \rangle^{1/2} \leq 573 \text{ km/s}$.

4. Even though we plan to discuss elsewhere the implications of these results for direct and indirect detection of dark matter, we may note here that the range in expected signals is large. The signals for direct detection are directly proportional to $\rho_{DM}(R_\odot)$ and increase at least linearly with $\langle v_{DM}^2(R_\odot) \rangle^{1/2}$, so that the allowed rate may vary at least by ~ 8 , even for detectors with very low threshold. The indirect experiments focus usually on detecting annihilation or decay of dark matter from the central regions of the Galaxy. These rates, proportional to $\rho_{DM}^2(0)$ and $\rho_{DM}(0)$, span a range of 400 and 20 respectively.

5. It is interesting to see if there exists any correlation between different parameters in these models that generally fit the rotation curves within the solar circle.

- (a) The correlation between the central density ρ_{DM0} and the values of the σ_{DM} parameter is shown in Fig. 22. Except for an initial decrease of σ_{DM} as ρ_{DM0} increases from very small values, the value of σ levels off around $\sim 200 \text{ km/s}$.
- (b) Similarly, the escape velocity from the center of the Galaxy stays around $\sim 900 \text{ km/s}$ for most values of ρ_{DM0} (see Fig. 23). Correspondingly, the escape from the location of the sun always stays around $\sim 600 \text{ km/s}$ (see Fig. 24).
- (c) The root-mean-square velocities of the dark matter particles $\langle v_{DM}^2(R_\odot) \rangle^{1/2}$ near the solar system stays nearly flat with respect to ρ_{DM0} (see Fig. 25). On the other hand, $\rho_{DM}(R_\odot)$ decreases as ρ_{DM0} increases as shown in Fig. 26.
- (d) The value of $\rho_{DM}(R_\odot)$ increases statistically with increasing $\langle v_{DM}^2(R_\odot) \rangle^{1/2}$ as shown in Fig. 27, thereby increasing the range of expectation of event rates in direct detection experiments.

6. After solving Poisson's equation, the potential at every point in the Galaxy is known. It is therefore possible to calculate the force profile in any direction. In Figs. 28-30,

TABLE I: Allowed dark matter models for $\Sigma_{d,\odot}=40 \text{ M}_\odot/\text{pc}^2$: Here the upper and lower limits in σ_{DM} are shown for each choice of ρ_{DM0} and Ψ_0/σ_{DM}^2 . The limits are found to encompass the entire allowed parameter space for $\Sigma_{d,\odot}=40 \text{ M}_\odot/\text{pc}^2$. The bold rows correspond to the most probable models (greatest L) from the BHB/BS analysis.

ρ_{DM0}	Ψ_0/σ_{DM}^2	σ_{DM}	$v_c(R_\odot)$	$< v_{DM}^2(R_\odot) >^{1/2}$	$\rho_{DM}(R_\odot)$	$v_{esc}(0)$	$v_{esc}(R_\odot)$	L
250	11	195	226.4	477.6	0.572	914.6	616.5	0.374
—	—	210	261.9	533.5	0.853	985.0	688.7	0.635
500	12	185	220.2	459.5	0.490	906.3	593.3	0.374
—	—	200	256.1	515.8	0.746	979.8	665.9	0.645

the vertical force profile at the Solar location is shown for the entire range of dark matter models allowed by the observations of the rotation curve. In principle, the motions of stars above the Galactic plane at R_\odot could be used to further constrain the dark matter parameters. In Fig. 31, the vertical force profile at the Galactic center is shown for the most-likely models from the BHB and BS analysis for the $\Sigma_{d,\odot} = 40 \text{ M}_\odot \text{ pc}^{-2}$ and $\Sigma_{d,\odot} = 70 \text{ M}_\odot \text{ pc}^{-2}$ disks. The dark matter phase-space distribution parameters for these two models are the same: $\rho_{DM0} = 500 \text{ GeV}/\text{cm}^3$ and $\sigma_{DM}^2 = 200 \text{ km/s}$. The difference in the vertical force profiles at the Galactic center come solely from the difference in disk surface densities. In Fig. 32, the radial force profile in the Galactic plane is shown for the same two dark matter models as in Fig. 31, and the difference between the force profiles in the plane of the Galaxy is negligible.

7. The parameters of the models that fall centrally on the rotation curve are given in Table IV. The corresponding rotation curves are shown in Figs. 33 and 34.

B. Comparison with the Distributions of BHB and BS Stars

The BHB and BS stars, with their distribution extending up to $\sim 90 \text{ kpc}$, serve as tracers of the gravitational potential of the Galaxy, even though they contribute negligibly to the potential. Since only their radial velocities are well determined, we will first write down their radial distribution function under the assumption that their PSD function follows the King distribution such as that given in eq. 13. This is achieved by writing $\Psi(r) = \frac{1}{2}v_{esc}^2(r)$

TABLE II: Allowed dark matter models for $\Sigma_{d,\odot}=70 \text{ M}_\odot/\text{pc}^2$: Here the upper and lower limits in σ_{DM} are shown for each choice of ρ_{DM0} and Ψ_0/σ_{DM}^2 . The limits are found to encompass the entire allowed parameter space for $\Sigma_{d,\odot}=70 \text{ M}_\odot/\text{pc}^2$. The bold rows correspond to the most probable models (greatest L) from the BHB/BS analysis.

ρ_{DM0}	Ψ_0/σ_{DM}^2	σ_{DM}	$v_c(R_\odot)$	$< v_{DM}^2(R_\odot) >^{1/2}$	$\rho_{DM}(R_\odot)$	$v_{esc}(0)$	$v_{esc}(R_\odot)$	L
25	7	235	220.6	444.2	0.164	879.3	573.4	0.087
—	—	270	263.4	573	0.844	1010	739.7	0.557
50	8	215	219.7	418.2	0.286	860	539.9	0
—	—	245	264.4	535.3	0.759	980	691	0.336
75	9	205	219.9	427.9	0.280	869.7	552.5	0.119
—	—	230	259.8	529.6	0.681	975.8	683.7	0.576
100	9	200	218.9	399.7	0.260	848.5	516	0
—	—	225	261.3	501.7	0.669	954.6	647.6	0.165
250	11	185	218.8	415.2	0.240	867.7	536.1	0.180
—	—	205	255.6	500.7	0.556	961.5	646.4	0.640
500	12	180	222.3	418.7	0.249	881.8	540.6	0.279
—	—	200	261	502.3	0.553	979.8	648.5	0.690

and integrating the PSD function over the transverse velocities:

$$F_B(r, v_r) = \frac{\rho_B}{(2\pi\sigma_B^2)^{3/2}} \int_0^{v_{esc}^2(r)-v_r^2} \left[\exp\left(\frac{v_{esc}^2(r) - v_r^2 - v_\perp^2}{2\sigma_B^2}\right) - 1 \right] dv_r \pi dv_\perp^2 \quad (20)$$

$$= \frac{\pi\rho_B}{(2\pi\sigma_B^2)^{3/2}} \left\{ 2\sigma_B^2 \left[\exp\left(\frac{v_{esc}^2(r) - v_r^2}{2\sigma_B^2}\right) - 1 \right] - (v_{esc}^2(r) - v_r^2) \right\} \quad (21)$$

Further integration of eq. 21 over radial and radial velocity bins, $\Delta r(r_i)$ and $\Delta v_r(r_i, v_j)$ respectively, is carried out to facilitate comparison with the observational data, which are binned similarly. First, the radial distribution is obtained by integrating $F_B(r, v_r)$ over the radial velocities:

$$n_B(r) = \int_0^{v_{esc}(r)} F_B(r, v_r) dv_r \quad (22)$$

$$= \frac{\rho_B}{(2\pi\sigma_B^2)^{3/2}} \left[\frac{(2\pi\sigma_B^2)^{3/2}}{2} e^{v_{esc}^2(r)/2\sigma_B^2} \text{erf}\left(\frac{v_{esc}(r)}{\sqrt{2\sigma_B^2}}\right) - \frac{2\pi}{3} v_{esc}^3(r) - 2\pi\sigma_B^2 v_{esc}(r) \right]. \quad (23)$$

We may now integrate $4\pi r^2 n_B(r)$ in the range Δr centered at various r_i to get $\Delta N(r_i)$ for comparison with the observations. A single choice for the parameter ρ_B should, in principle, fit the total number of stars in each radial bin when we include all the stars in each at that location irrespective of their velocities. Unfortunately, as described below, this does not happen, and the observed number of stars, especially at galactocentric distances below $\sim 20 - 30 \text{ kpc}$, fall short of the theoretical expectation. The most likely explanation for this is that the catalogues of the observations are incomplete in these regions. In fact, the radial

TABLE III: Allowed dark matter models for $\Sigma_{d,\odot}=100 \text{ M}_\odot/\text{pc}^2$: Here the upper and lower limits in σ_{DM} are shown for each choice of ρ_{DM0} and Ψ_0/σ_{DM}^2 . The limits are found to encompass the entire allowed parameter space for $\Sigma_{d,\odot}=100 \text{ M}_\odot/\text{pc}^2$. The bold rows correspond to the most probable models (greatest L) from the BHB/BS analysis.

ρ_{DM0}	Ψ_0/σ_{DM}^2	σ_{DM}	$v_c(R_\odot)$	$< v_{DM}^2(R_\odot) >^{1/2}$	$\rho_{DM}(R_\odot)$	$v_{esc}(0)$	$v_{esc}(R_\odot)$	L
1	7	230	220	411.1	0.008	860.6	530.7	0.926
—	—	665	260.1	1851	0.577	2488	2390	0.768
5	9	195	220.1	367.4	0.008	827.3	474.3	0.108
—	—	200	220.1	395.1	0.011	848.5	510.1	0.975
—	—	330	260.8	941.2	0.534	1400	1215	0.768
10	10	180	219.9	336.1	0.006	805	433.9	0
—	—	190	220.7	396.1	0.014	849.7	511.4	0.975
—	—	285	259.8	826.3	0.493	1275	1067	0.768
25	12	165	219.8	340.3	0.004	808.3	439.3	0
—	—	175	220.7	405.1	0.012	857.3	523	0.951
—	—	250	261.7	777.1	0.479	1225	1003	0.768
50	13	160	220	349.7	0.005	815.8	451.4	0
—	—	170	221.2	415.6	0.015	866.8	536.5	0.906
—	—	230	261.3	724.9	0.442	1173	935.8	0.768
75	14	155	220	355	0.004	820.2	458.3	0
—	—	165	221.2	422.5	0.014	873.1	545.5	0.880
—	—	220	260.2	714.8	0.411	1164	922.8	0.768
100	15	150	219.8	356.5	0.003	821.6	460.2	0
—	—	155	220.2	392.4	0.006	849	506.5	1
—	—	215	261.2	725.9	0.407	1178	937.1	0.768
250	16	145	220.1	350.2	0.003	820.2	452.1	0
—	—	150	220.7	387.1	0.007	848.5	499.8	0.941
—	—	200	259.9	672.9	0.351	1131	868.7	0.768
500	17	140	221.3	338.7	0.002	816.3	437.2	0
—	—	150	222.3	413	0.011	874.6	533.1	0.926
—	—	195	263.5	666.4	0.349	1137	860.3	0.768
1000	21	125	223.9	320.1	0.0001	810.1	413.4	0
—	—	130	231.5	365.6	0.0005	842.5	472	0.951
—	—	185	256.3	722.2	0.248	1199	932.3	0.768

TABLE IV: Parameters of the models which best first the rotation curve are shown, corresponding to Figs. 33 and 34

ρ_{DM0}	Ψ_0/σ_{DM}^2	σ_{DM}	$v_c(R_\odot)$	$< v_{DM}^2(R_\odot) >^{1/2}$	$\rho_{DM}(R_\odot)$	$v_{esc}(0)$	$v_{esc}(R_\odot)$	L
$\Sigma_{d,\odot}=40 \text{ M}_\odot/\text{pc}^2$								
250	11	205	250.1	515.4	0.760	961.5	665.4	0.567
500	12	195	244.2	497.7	0.662	955.3	642.5	0.576
$\Sigma_{d,\odot}=70 \text{ M}_\odot/\text{pc}^2$								
25	7	255	244	520	0.573	954.1	671.3	0.382
50	8	235	248.3	498.3	0.582	940	643.3	0.182
75	9	220	242.7	490.8	0.505	933.4	633.6	0.435
100	9	215	243.1	463.1	0.489	912.2	597.8	0.041
250	11	200	245.6	480.7	0.470	938.1	620.6	0.571
500	12	195	250.7	482.8	0.473	955.3	623.3	0.640

distributions presented by Xue *et al.* [38] and Brown *et al.* [39] differ significantly from each other. We show in Fig. 35 the theoretical distribution of stars $N(r)$, where

$$N(r) = 4\pi r^2 n_B(r), \quad (24)$$

for the Brown *et al.* and Xue *et al.* data separately. The σ_B values were chosen to be 115 km/s and 106 km/s for fitting the Brown *et al.* and Xue *et al.* data respectively beyond ~ 25 kpc along with arbitrary normalizations to the total number of stars in the particular radial bin. The escape velocity profile was taken from the best-fit model in the $\Sigma_{d,\odot} = 70$ M_\odot pc $^{-2}$ disk where $\rho_{DM0} = 500$ GeV/cm 3 and $\sigma_{DM} = 200$ km/s. In order to proceed further, we normalize $\Delta N(r_i)$ at each radial bin and compare the theoretical distribution of radial velocities with the observations in Figs. 6-11. Here again, a range of parameters fit the observations.

In order to find the best fitting model, we define f_{ij} as the theoretical expectation for the number of stars in the radial bins at r_i and the velocity bin at v_{rj} . If n_{ij} is the actual number of stars observed in this bin, then using Poisson statistics, we may define the likelihood function for each model to be

$$L = \prod_{ij} \frac{e^{-f_{ij}} f_{ij}^{n_{ij}}}{n_{ij}!}. \quad (25)$$

After the likelihoods for all the models were calculated, they were normalized to the model with the greatest likelihood, the $\rho_{DM0} = 100$ GeV/cm 3 , $\sigma_{DM} = 155$ km/s model for the $\Sigma_{d,\odot} = 100$ M_\odot pc $^{-2}$ disk. The dark matter models with the greatest likelihood L for each choice of central dark matter density are shown as bold in the data tables.

If we neglect the $\Sigma_{d,\odot} = 100$ M_\odot pc $^{-2}$ disk, as it lies outside observational constraints, and focus instead on the other two disks, the most probable models for both the $\Sigma_{d,\odot} = 40$ M_\odot pc $^{-2}$ and $\Sigma_{d,\odot} = 70$ M_\odot pc $^{-2}$ disks occur for the same set of dark matter parameters, $\rho_{DM0} = 500$ GeV/cm 3 , $\Psi_0/\sigma_{DM}^2=12$, and $\sigma_{DM} = 200$ km/s. Though the parameters of their phase-space distribution are identical, the difference in their visible matter distribution causes the value of the local dark matter density at R_\odot to vary from 0.55-0.75 GeV/cm 3 . We also note that the most probable models with $\rho_{DM0} = 250$ GeV/cm 3 are similar in likelihood to the most probable models with $\rho_{DM0} = 500$ GeV/cm 3 . Models with very low likelihood values did not have large enough spatial extent to reproduce the BHB/BS distributions.

The dark matter models with the greatest likelihood from the BHB/BS analysis are not the same models that best fit the rotation curve. In Table IV, it is shown that the models

that best fit the rotation curve have a range of values of $L = 0.04 - 0.64$. The models best fitting the rotation curve and have the highest value of L are the $\rho_{DM0} = 500 \text{ GeV/cm}^3$, $\sigma_{DM} = 195$ models for both the lighter disks.

VI. DISCUSSION

While the observations of the rotation curve remain the best probe of the Galactic potential out to $\sim 20 \text{ kpc}$, the high dispersion in the observed rotation speeds at large distances does not allow a precise determination of the dark matter phase-space distribution. If models are considered where $v_c(R_\odot) = 220 - 260 \text{ km/s}$, a wide range in the parameters of the dark matter phase-space distribution is allowed, as shown in Tables I-III and Figs. 22-27. Even when the rotation curve is confined to lie within a narrow band encompassing 2/3 of the observed data, a wide range of parameters is still allowed because of the uncertainties in the determination of the mass of the visible matter in the Galactic disk: $\rho_{DM0} = 25 - 500 \text{ GeV/cm}^3$, $\rho_{DM}(R_\odot) = 0.47 - 0.76 \text{ GeV/cm}^3$, and $\langle v_{DM}^2(R_\odot) \rangle^{1/2} = 463 - 520 \text{ km/s}$.

Analysis of the distributions of BHB and BS stars was found not to help in significantly constraining the range of allowed parameters for the dark matter phase-space distribution. Figures 16-18 show that for the $\Sigma_{d,\odot} = 40$ and $70 \text{ M}_\odot \text{ pc}^{-2}$ disks, the dark matter models with the highest likelihood L produce rotation curves that are on the highest ended of the those allowed by the initial rotation curve analysis, and these rotation curves lie just above the band containing 2/3 of the observational data. For the $\Sigma_{d,\odot} = 100 \text{ M}_\odot \text{ pc}^{-2}$ disk, the most-probable models do not agree with the rotation curve observations and lie far under the observations beyond $\sim 10 \text{ kpc}$.

The models providing the best fit for both disks with surface densities within observational constraints to both the rotation curve and the BHB/BS distributions occur for the same dark matter phase-space distribution parameters: $\rho_{DM0} = 500 \text{ GeV/cm}^3$, $\Psi_0/\sigma_{DM}^2 = 12$, and $\sigma_{DM} = 195 \text{ km/s}$. The parameters of the dark matter distribution for these models lie in the range $\langle v^2(R_\odot)_{DM} \rangle^{1/2} = 483 - 498 \text{ km/s}$ and $\rho_{DM}(R_\odot) = 0.47 - 0.66 \text{ GeV/cm}^3$, and this dispersion is essentially attributable to the range in the assumed surface density of the disk. This range of local dark matter densities is notably higher than the Standard Halo Model. The effect this increase has on the expected rates of direct and indirect detection predictions will be discussed in a companion paper.

Though we did not include these observations in this study, it may be possible to further constrain the dark matter phase-space distribution by comparing the vertical force exerted by the Galactic potential at R_\odot to the stellar observations perpendicular to the plane in the Solar neighborhood. We have shown the expected vertical force profiles at R_\odot in Figs. 28-30.

Better observations of the distance of the Sun from the Galactic center and the value of the rotation speed at the Solar circle as well as observations of the rotation curve beyond R_\odot , especially at distances beyond 20 kpc, would allow for better constraints on the phase-space distribution of dark matter. The currently observed distributions of BHB and BS stars have large uncertainties as to their absolute spatial densities and do not place tight bounds on the dark matter phase-space distribution on their own. This was shown by the wide range of dark matter models that adequately reproduced the velocity distributions at various distances compiled by Xue *et al.* and Brown *et al.* The wide range of allowed parameters shows that more precise astronomical observations, especially pertaining to the surface mass density of the disk, are needed to narrow down the parameters of the phase-space distribution of dark matter and to be able to correctly interpret the results of direct and indirect dark matter detection experiments. As far as the present status of the observations are concerned, assuming the surface density of the Galactic disk is $\sim 55 \text{ M}_\odot/\text{pc}^2$, a value in the middle of the observational constraints, the best choice for the parameters of Galactic dark matter are the following: $\rho_{DM0} \approx 500 \text{ GeV}/\text{cm}^3$, $\rho_{DM}(R_\odot) \approx 0.6 \text{ GeV}/\text{cm}^3$, and $\langle v_{DM}^2(R_\odot) \rangle^{1/2} \approx 490 \text{ km/s}$.

-
- [1] Bahcall, J. N., Schmidt, M., & Soneira, R. M. 1983, AJ, 265, 730
 - [2] Caldwell, J. A. R. & Ostriker, J. P. 1981, AJ, 251, 61
 - [3] Turner, M. S. 1986, Phys. Rev. D, 33, 889
 - [4] Flores, R. A. 1988, Phys. Lett. B, 215, 73
 - [5] Bovy, J. & Tremaine, S. 2012, arXiv:1205.4033
 - [6] Kuhlen, M. et al., 2010, JACP, 02, 030
 - [7] McMillan, P. J. 2011, MNRAS, 414, 2446
 - [8] Libeskind, N. I. et al., 2010, MNRAS, 411, 1525

- [9] Cowsik, R., Ratnam, C., & Bhattacharjee, P. 1996, PRL, 76, 3886
- [10] Helmi, A. 2008, Astron. Astrophys. Rev., 15, 145
- [11] Freeman, K. C. 1970, ApJ, 160, 811
- [12] Cabrera-Lavers, A., Garzón, F., & Hammersley, P. L. 2005, A&A, 433, 173
- [13] Kuijken, K. & Gilmore, G. 1989, MNRAS, 239, 605
- [14] Kuijken, K. & Gilmore, G. 1991, ApJ, 367, L9
- [15] Flynn, C. & Fuchs, B. 1994, MNRAS, 270, 471
- [16] Gould, A., Bahcall, J. N., & Flynn, C. 1996, ApJ, 465, 759
- [17] Korchagin, V. I., *et al.* 2003, ApJ, 126, 2896
- [18] Siebert, A., Bienaymé, O, and Soubiran, C. 2003, A&A, 399, 531
- [19] Holmberg, J. & Flynn, C. 2004, MNRAS, 352, 440
- [20] Flynn, C., *et al.* 2006, MNRAS, 372, 1149
- [21] Weber, W. & de Boer, W. 2010, A&A, 509, A25
- [22] Ojha, D. K. 2001, MNRAS, 322, 426
- [23] Reid, N. & Majewski, S. R. 1993, ApJ, 409, 635
- [24] Buser, R., Rong, J., & Karaali, S. 1999, A&A, 348, 98
- [25] Spagna, A., *et al.* 1996, A&A, 313, L21
- [26] Ng, Y. K., *et al.* 1997, A&A, 324, 65
- [27] Larsen, J. A. & Humphreys, R. M. 2003, AJ, 125, 1958
- [28] Robin, A. C., *et al.* 1996, A&A, 305, 125
- [29] Siegel, M. H., *et al.* 2002, ApJ, 578, 151
- [30] Carollo, D., *et al.* 2010, ApJ, 712, 692
- [31] Jurić, M., *et al.* 2008, ApJ, 673, 864
- [32] Sofue, Y., Honma, M., & Omodaka, T. 2009, PASJ, 61, 227
- [33] Mo, H., van den Bosch, F., & White, S. 2010, *Galaxy Formation and Evolution*, Cambridge University Press, Cambridge
- [34] Dejonghe, H. 1987, MNRAS, 224, 12
- [35] Minniti, D., *et al.* 1992, ApJ, 393, L47
- [36] Rich, M., *et al.* 2007, ApJ, 658, L29
- [37] Blum, R. D., *et al.* 1995, ApJ, 449, 623
- [38] Xue, X. X., *et al.* 2008, ApJ, 684, 1143

- [39] Brown, W. R., *et al.* 2010, ApJ, 139, 59
- [40] Burton, W. B. & Gordon, M. A. 1978, A&A, 63, 7
- [41] Blitz, L., Fich, M., & Stark, A. A. 1982, ApJS, 49, 183
- [42] Schneider, S. E. & Terzian, Y. 1983, ApJL, 274, L61
- [43] Clemens, D. P. 1985, ApJ, 295, 422
- [44] Fich, M., Blitz, L., & Stark, A. A. 1989, ApJ, 342, 272
- [45] Burton, W. B. & Liszt, H. S. 1993, A&A, 274, 765
- [46] Turbide, L. & Moffat, A. F. J. 1993, AJ, 105, 1831
- [47] Honma, M. & Sofue, Y. 1997, PASJ, 49, 453
- [48] Pont, F., *et al.* 1997, A&A, 318, 416
- [49] Honma, M., *et al.* 2007, PASJ, 59, 889
- [50] McClure-Griffiths, N. M. & Dickey, J. M. 2007, ApJ, 671, 427
- [51] Oh, C. S., *et al.* 2010, PASJ, 62, 101
- [52] Stepanishchev, A. S. & Bobylev, V. V. 2011, Astron. Lett., 37, 254
- [53] Demers, S. & Battinelli, P. 2007, A&A, 473, 143
- [54] Avedisova, V.S. 2005, Astron. Rep. 49, 435
- [55] Ghez, A. M., *et al.* 2008, ApJ, 689, 1044
- [56] Gillessen, S., *et al.* 2009, ApJ, 692, 1075
- [57] Reid, M. J. 2009, Int. J. Mod. Phys. D, 18, 889
- [58] Reid, M. J., *et al.* 2008, ApJ, 700, 137
- [59] Brunthaler, A., *et al.* 2011, Astron. Nachr., 332, 461
- [60] Reid, M. J. & Brunthaler, A. 2004, ApJ, 616, 872
- [61] McMillan, P. J. & Binney, J. J. 2010, MNRAS, 402, 934
- [62] Schönrich, R., Binney, J. & Dehnen, W. 2010, MNRAS, 403, 1829
- [63] Binney, J. & Tremaine, S. 2008, *Galactic Dynamics*, Princeton University Press, Princeton
- [64] Cowsik, R., *et al.* 2007, New Astron., 12, 507
- [65] Chaudhury, S., Bhattacharjee, P., & Cowsik, R. 2010, JCAP, 09, 020
- [66] Wilson, C. P. 1975, ApJ, 80, 175
- [67] Prendergast, K. H. & Tomer, E. 1970, AJ, 75, 674

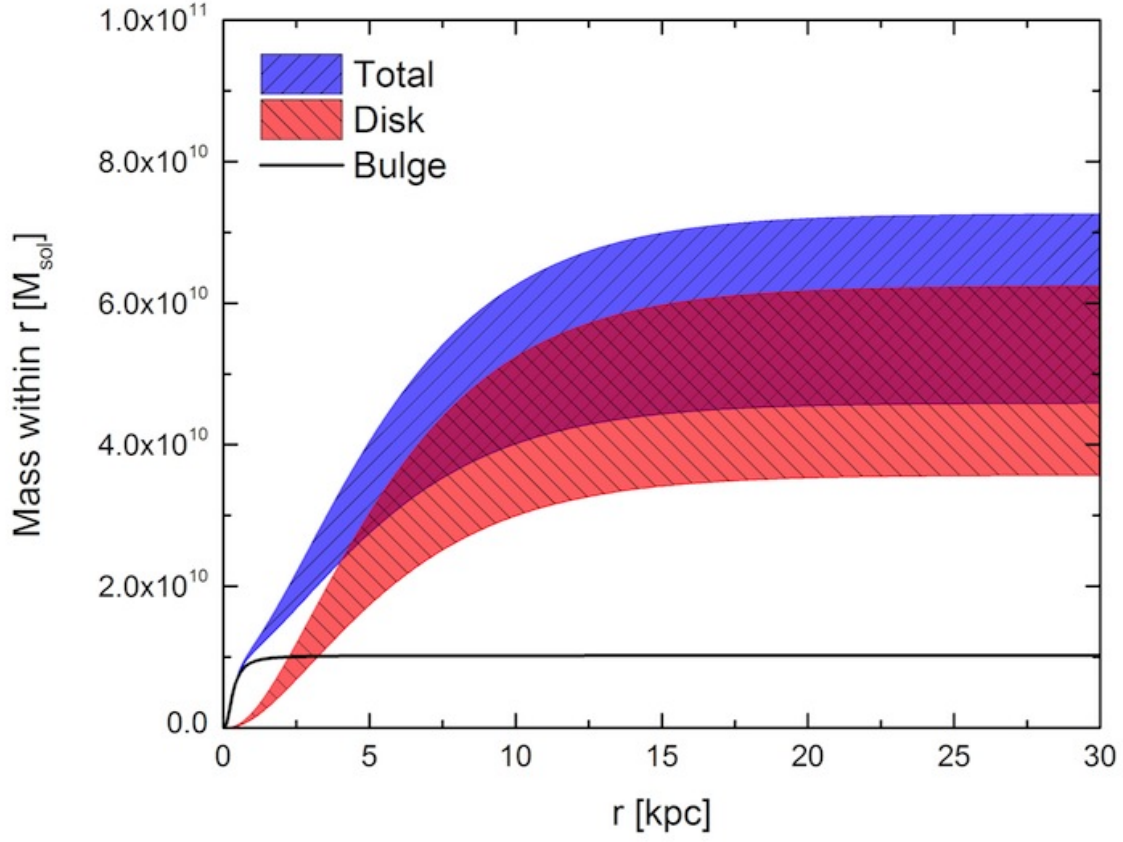


FIG. 1: The mass profiles of the Plummer bulge (eq. 8) and double-exponential disk (eq. 3) as well as their sum are plotted as a function of distance from the Galactic center. The range of masses for the disk is shown for $\Sigma_{d,\odot} = 40 - 70 \text{ M}_{\odot} \text{ pc}^{-2}$.

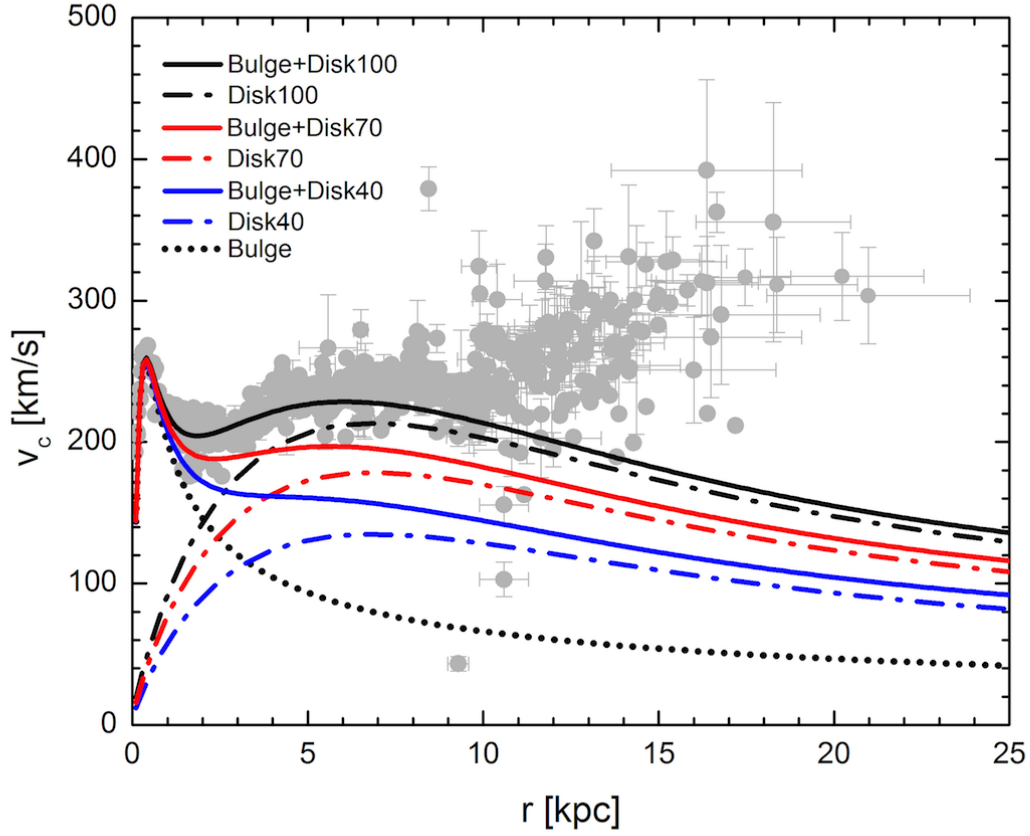


FIG. 2: The rotation curve predicted by the visible matter components alone is shown along with the shaded observations. Observational constraints on the local visible matter surface density indicate that some dark matter is needed to reconcile the dynamics from visible matter alone with the rotation curve starting at about 1 kpc, and dark matter will become the dominant component at about 10 kpc.

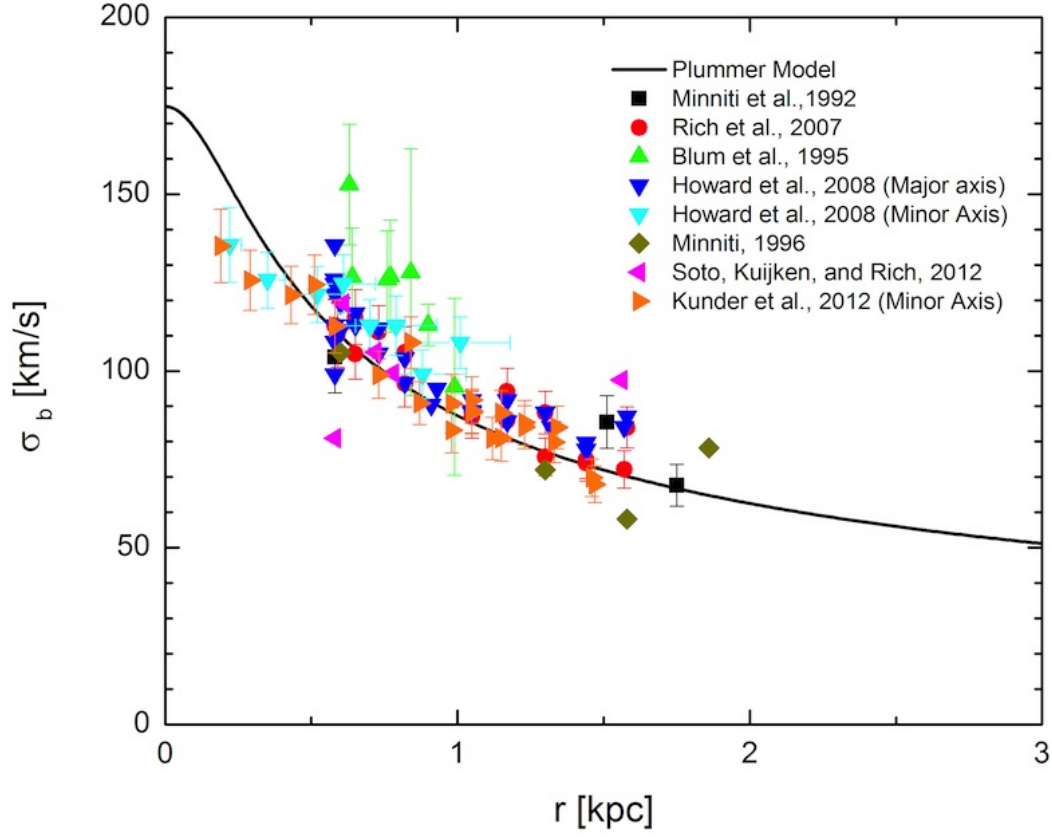


FIG. 3: The velocity dispersion expected from the bulge (eq. 10) is plotted along with K and M giant observations [35–37]. The agreement between the observations and the prediction from the Plummer profile implies that the mass distribution of the bulge can be adequately fit by a Plummer profile in the region of interest.

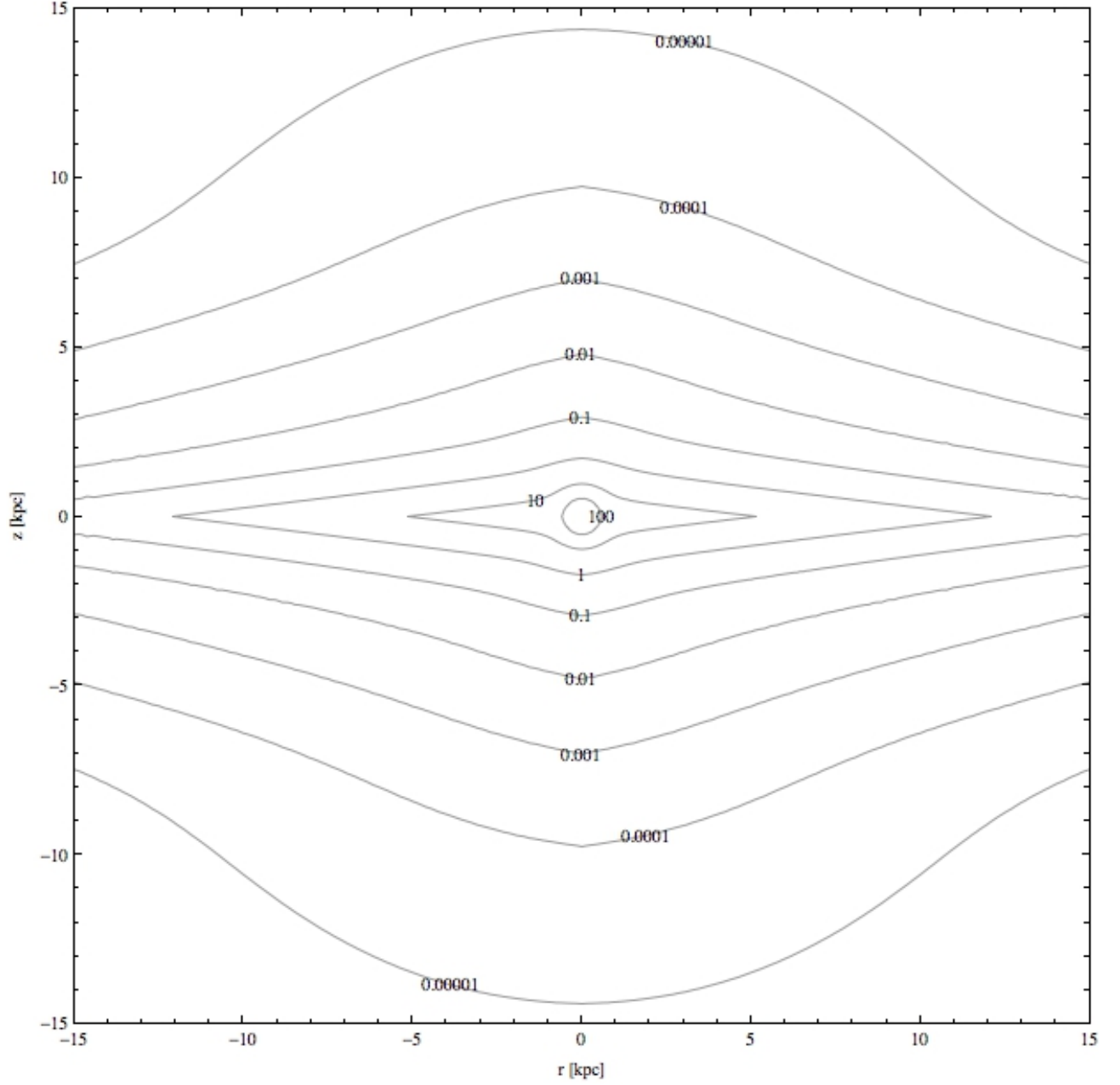


FIG. 4: The density (in GeV/cm^3) of the visible Milky Way is shown as an edge-on contour plot. The disk is assumed to have a surface density of $\Sigma_{d,\odot}=70 \text{ M}_\odot \text{ pc}^{-2}$.

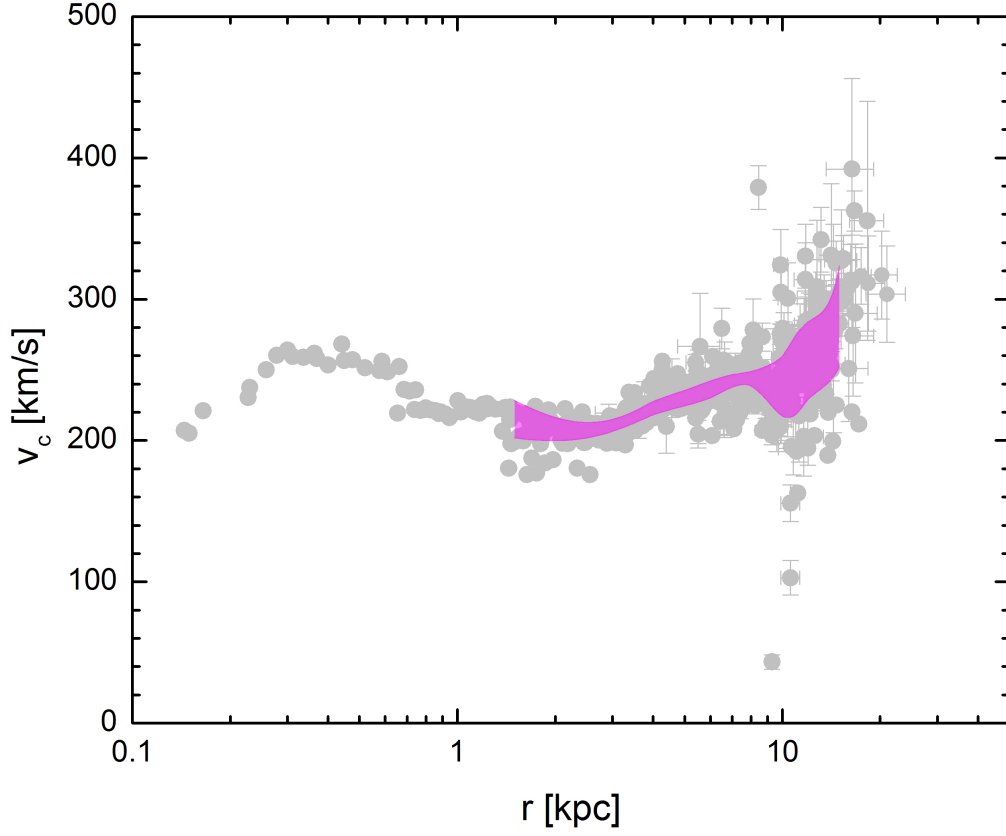


FIG. 5: Observations of the rotation curve [40–52] are plotted after rescaling all the data using $R_{\odot} = 8.3$ kpc and $\Theta_{\odot} = 240$ km/s and adjusting for the current measurements of the peculiar motion of the Sun. The magenta band indicates there region where $\frac{2}{3}$ of the points lie within 1 kpc radial bins.

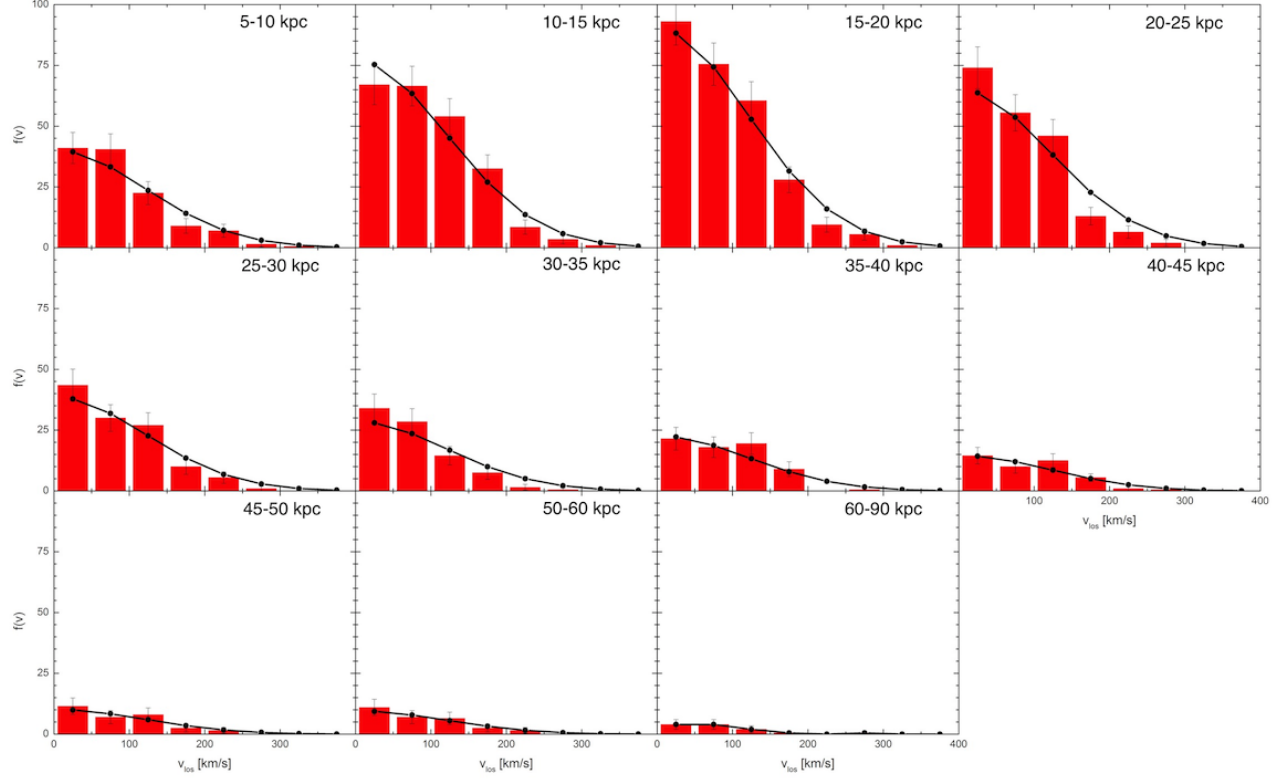


FIG. 6: The line-of-sight velocity distribution of BHB stars from Xue *et al.* [38] is presented in radial velocity and radial bins in the red histogram with error bars. The distribution computed for the best-fit dark matter model for the $\Sigma_{d,\odot}=40 \text{ M}_\odot/\text{pc}^2$ disk is shown as points, connected for clarity. In this model, $\rho_{DM0} = 500 \text{ GeV}/\text{cm}^3$, $\sigma_{DM} = 200 \text{ km/s}$, $\Phi_0/\sigma_{DM}^2=12$ and $\sigma_{BHB} = 106 \text{ km/s}$.

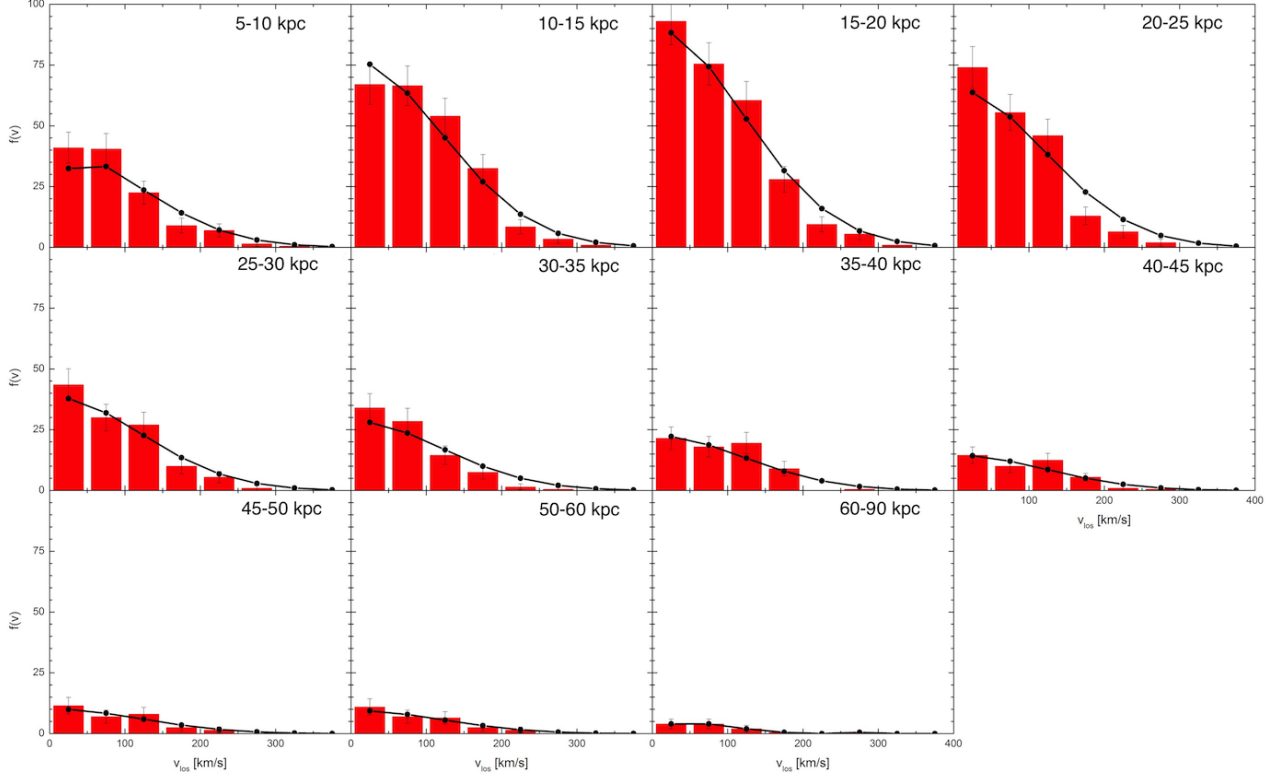


FIG. 7: The line-of-sight velocity distribution of BHB stars from Xue *et al.* [38] is presented in radial velocity and radial bins in the red histogram with error bars. The distribution computed for the best-fit dark matter model for the $\Sigma_{d,\odot}=70 \text{ M}_\odot/\text{pc}^2$ disk is shown as points, connected for clarity. In this model, $\rho_{DM0} = 500 \text{ GeV}/\text{cm}^3$, $\sigma_{DM} = 200 \text{ km/s}$, $\Phi_0/\sigma_{DM}^2=12$ and $\sigma_{BHB} = 106 \text{ km/s}$.

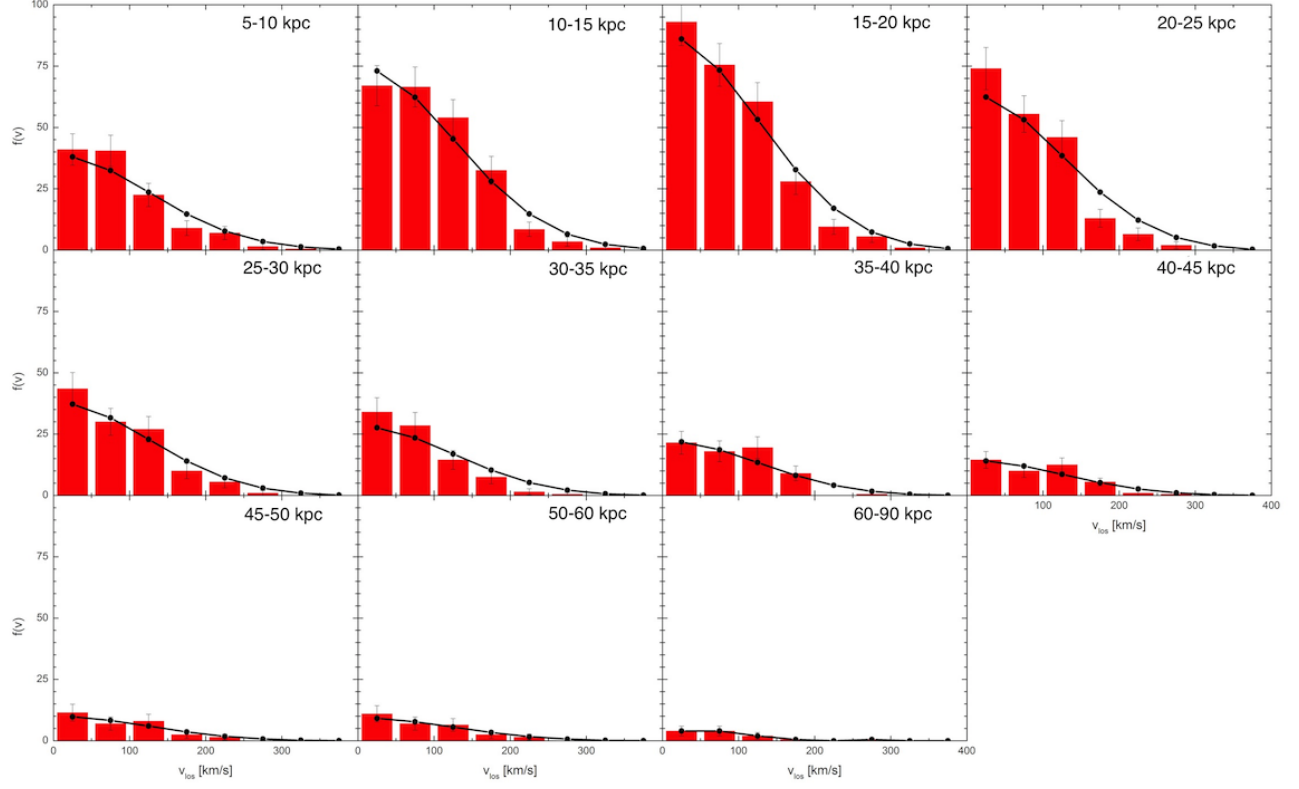


FIG. 8: The line-of-sight velocity distribution of BHB stars from Xue *et al.* [38] is presented in radial velocity and radial bins in the red histogram with error bars. The distribution computed for the best-fit dark matter model for the $\Sigma_{d,\odot}=100 \text{ M}_\odot/\text{pc}^2$ disk is shown as points, connected for clarity. In this model, $\rho_{DM0} = 100 \text{ GeV}/\text{cm}^3$, $\sigma_{DM} = 155 \text{ km/s}$, $\Phi_0/\sigma_{DM}^2=15$ and $\sigma_{BHB} = 106 \text{ km/s}$.

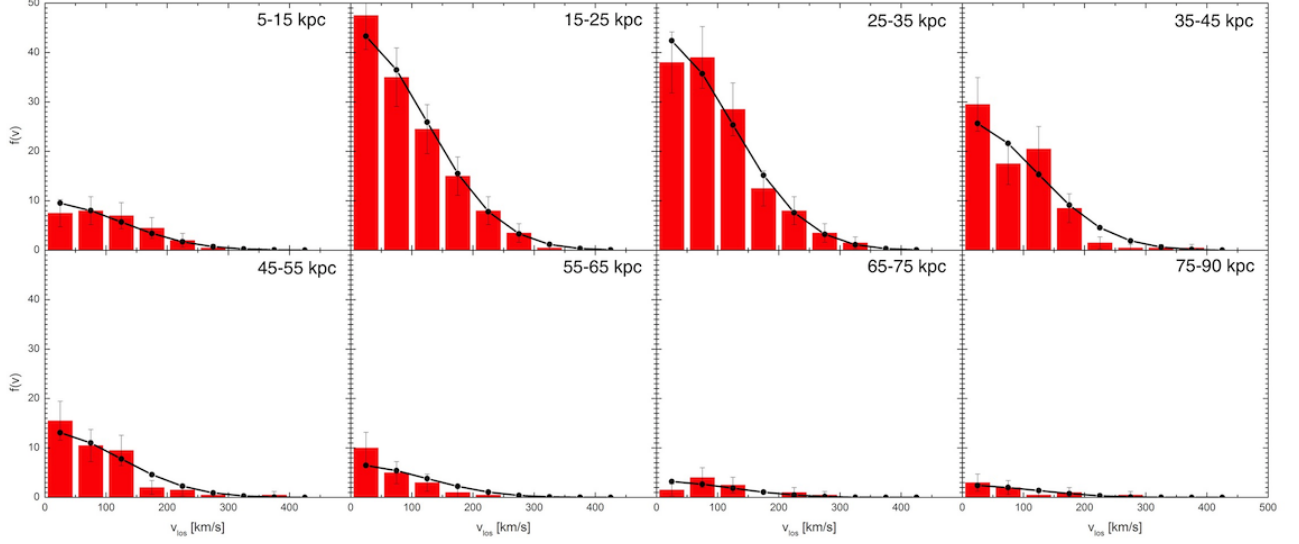


FIG. 9: The line-of-sight velocity distribution of BHB and BS stars from Brown *et al.* [39] is presented in radial velocity and radial bins in the red histogram with error bars. The distribution computed for the best-fit dark matter model for the $\Sigma_{d,\odot}=40 \text{ M}_\odot/\text{pc}^2$ disk is shown as points, connected for clarity. In this model, $\rho_{DM0} = 500 \text{ GeV}/\text{cm}^3$, $\sigma_{DM} = 200 \text{ km/s}$, $\Phi_0/\sigma_{DM}^2=12$ and $\sigma_{BHB,BS} = 115 \text{ km/s}$.

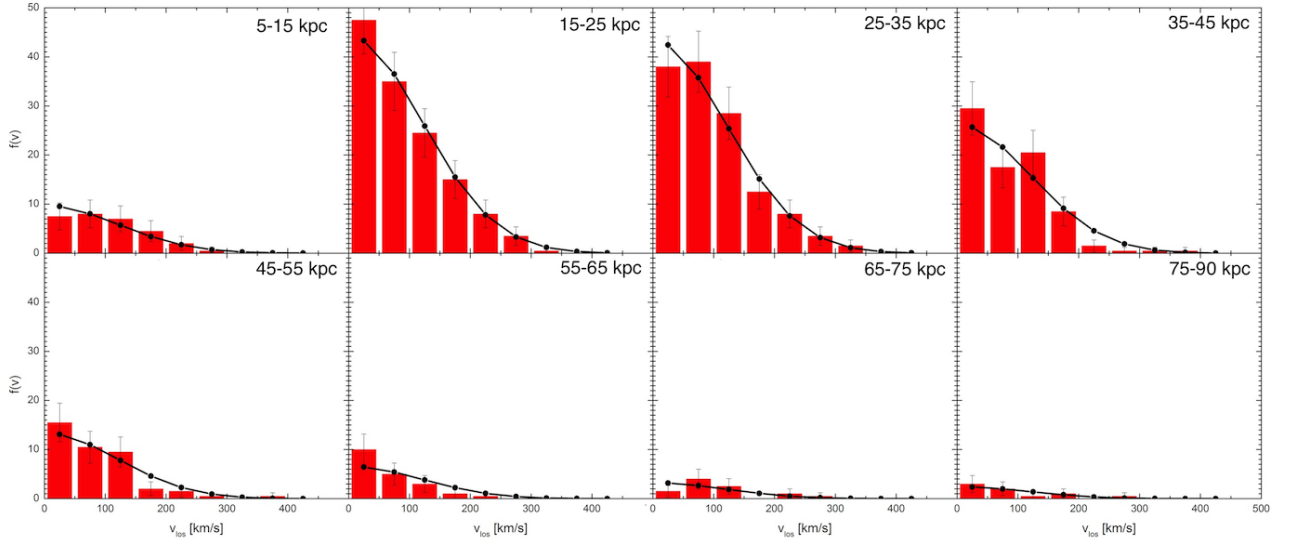


FIG. 10: The line-of-sight velocity distribution of BHB and BS stars from Brown *et al.* [39] is presented in radial velocity and radial bins in the red histogram with error bars. The distribution computed for the best-fit dark matter model for the $\Sigma_{d,\odot}=70 \text{ M}_\odot/\text{pc}^2$ disk is shown as points, connected for clarity. In this model, $\rho_{DM0} = 500 \text{ GeV}/\text{cm}^3$, $\sigma_{DM} = 200 \text{ km/s}$, $\Phi_0/\sigma_{DM}^2=12$ and $\sigma_{BHB,BS} = 115 \text{ km/s}$.

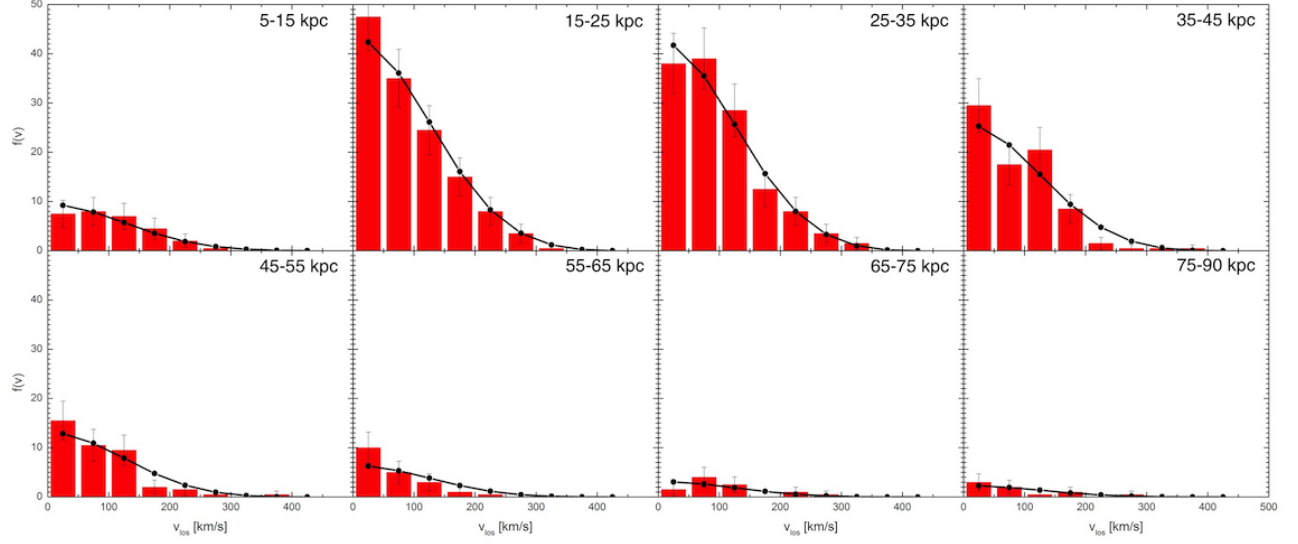


FIG. 11: The line-of-sight velocity distribution of BHB and BS stars from Brown *et al.* [39] is presented in radial velocity and radial bins in the red histogram with error bars. The distribution computed for the best-fit dark matter model for the $\Sigma_{d,\odot}=100 \text{ M}_{\odot}/\text{pc}^2$ disk is shown as points, connected for clarity. In this model, $\rho_{DM0} = 100 \text{ GeV}/\text{cm}^3$, $\sigma_{DM} = 155 \text{ km/s}$, $\Phi_0/\sigma_{DM}^2=15$ and $\sigma_{BHB,BS} = 115 \text{ km/s}$.

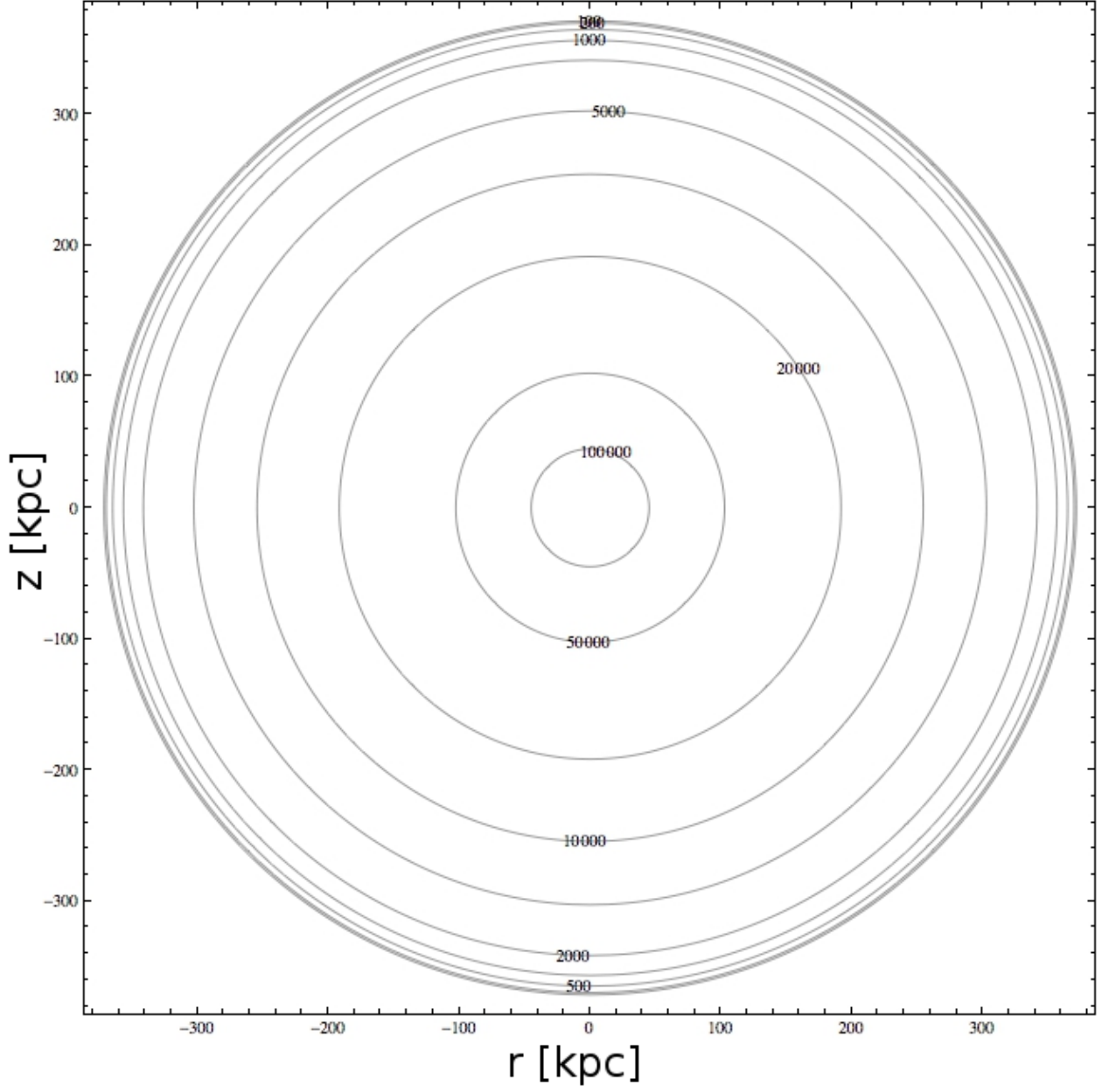


FIG. 12: The dark matter potential Ψ for the most probable dark matter model for the $\Sigma_{d,\odot}=70 \text{ M}_\odot/\text{pc}^2$ disk ($\rho_{DM0} = 500 \text{ GeV}/\text{cm}^3$, $\sigma_{DM} = 200 \text{ km/s}$, $\Phi_0/\sigma_{DM}^2=12$) is plotted as an edge-on contour plot. The potential is in units of $\text{km}^2 \text{s}^{-2}$.

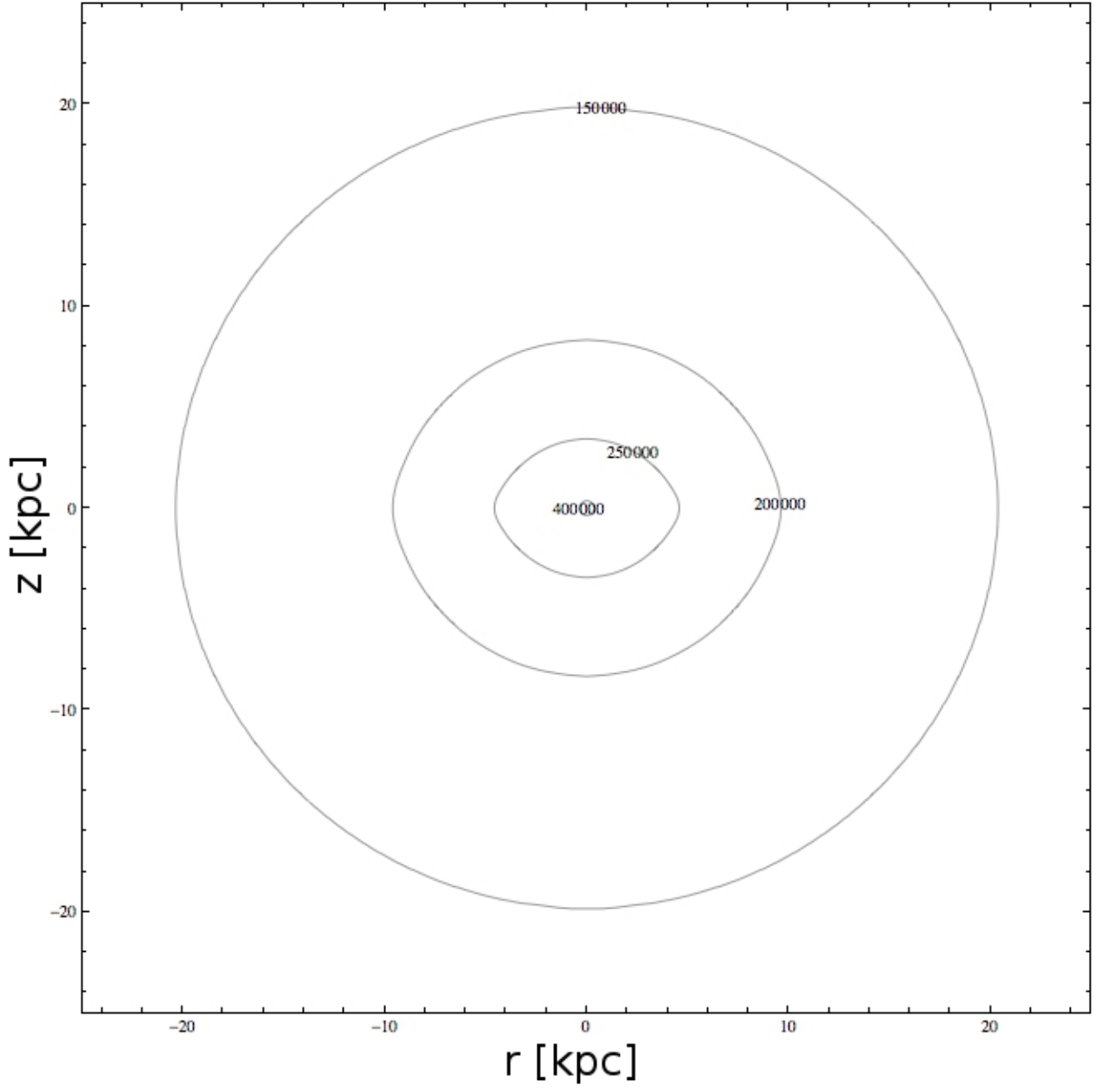


FIG. 13: The inner 25 kpc of Fig. 12.

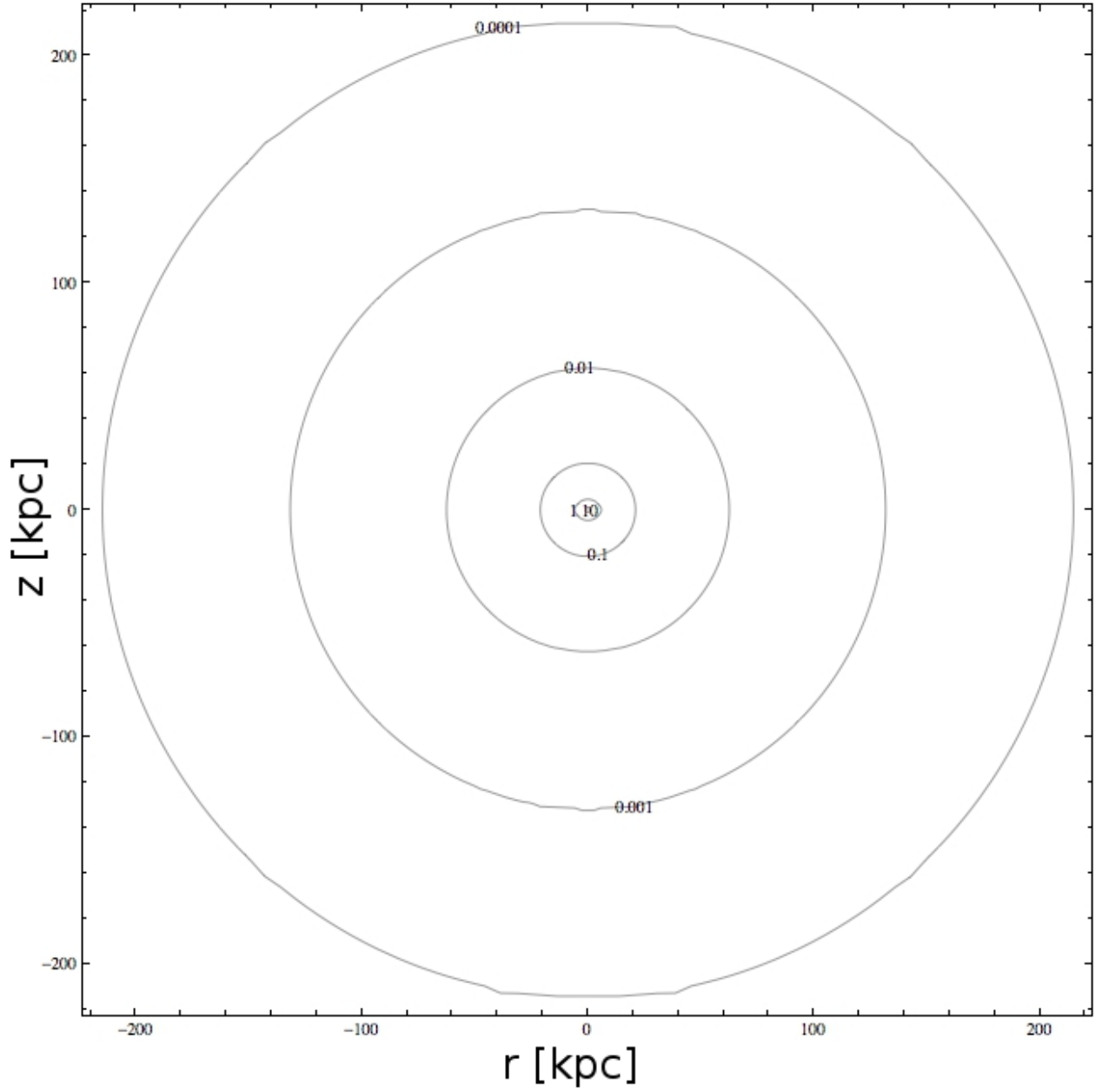


FIG. 14: The dark matter density ρ_{DM} (in units of GeV/cm^3) for the most probable dark matter model for the $\Sigma_{d,\odot}=70 \text{ M}_\odot/\text{pc}^2$ disk ($\rho_{DM0} = 500 \text{ GeV}/\text{cm}^3$, $\sigma_{DM} = 200 \text{ km/s}$, and $\Phi_0/\sigma_{DM}^2=12$) is shown as an edge-on contour plot. Any jaggedness on the contours are artifacts of the interpolation process.

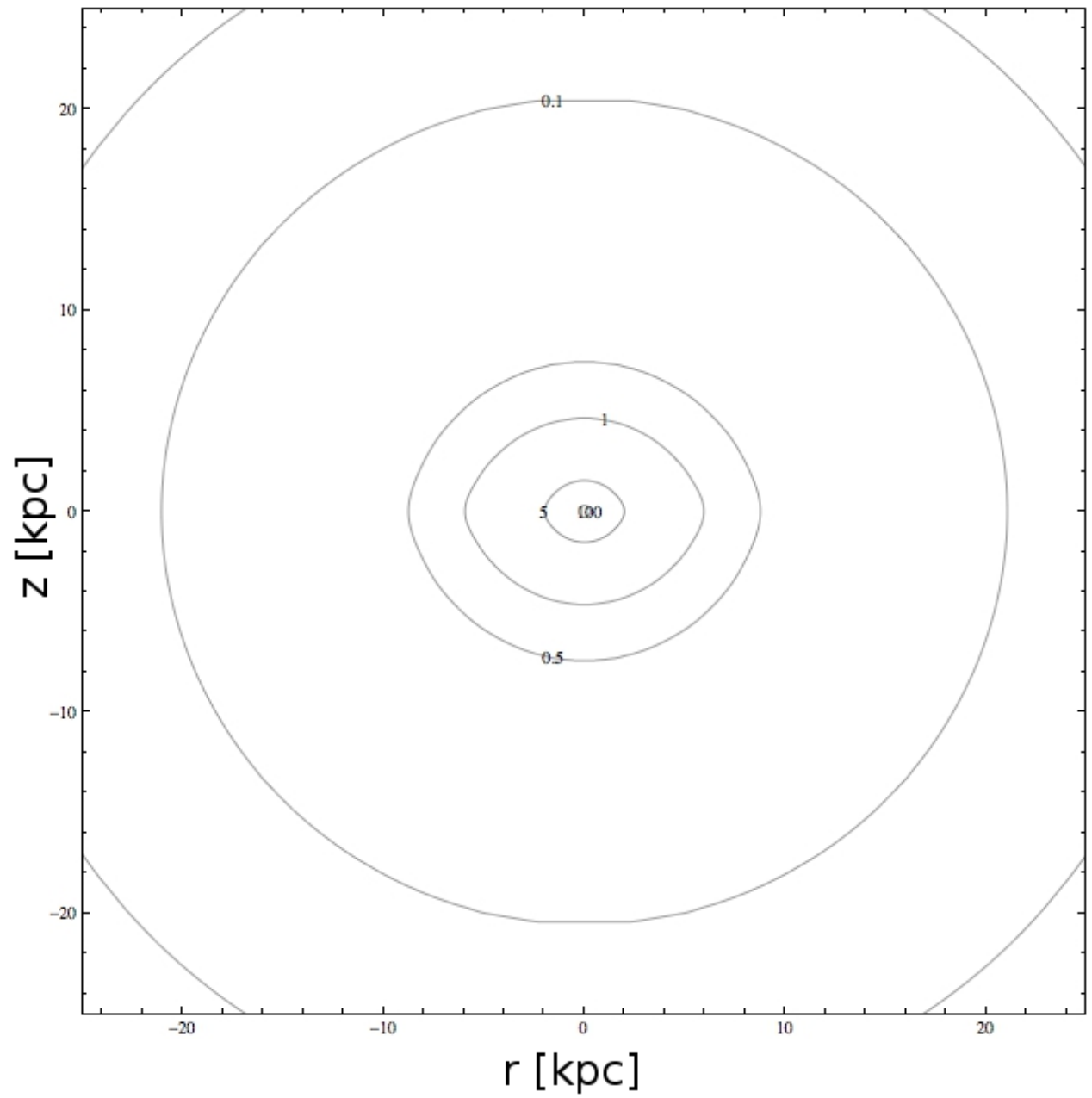


FIG. 15: The inner 25 kpc of Fig. 14.

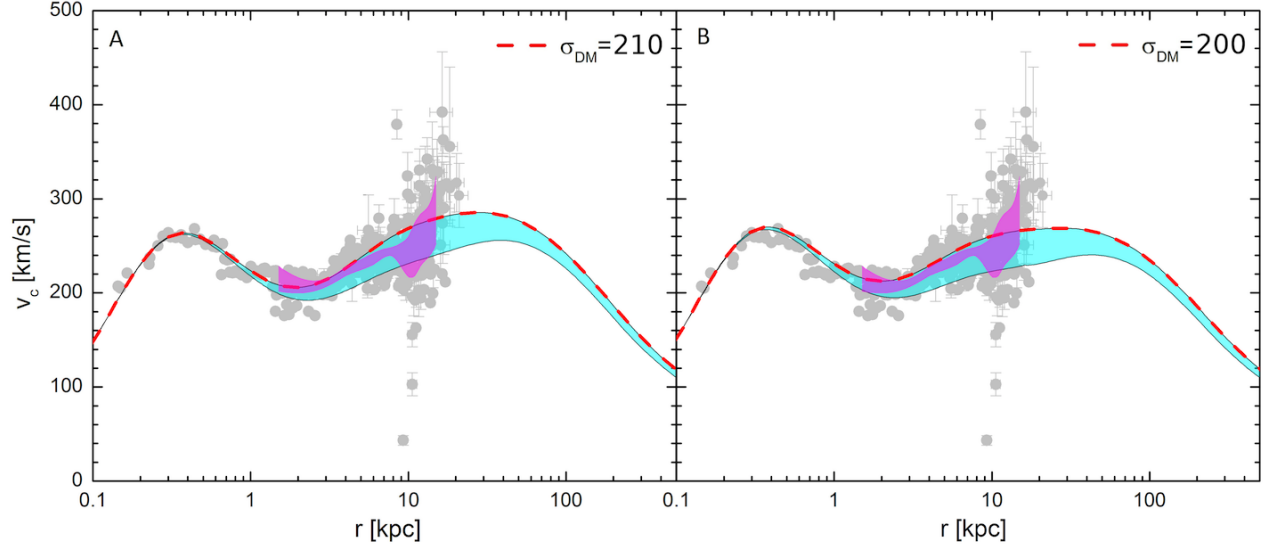


FIG. 16: The rotation curves for the range of dark matter models allowed by the constraint $v_c(R_\odot) = 220 - 260$ km/s are shown in blue for the lightest disk model where $\Sigma_{d,odot}=40$ M_\odot/pc^2 . The dashed line shows the maximum likelihood model for each choice of ρ_{DM0} (shown in bold in Table I): A) $\rho_{DM0}=250$ GeV/cm^3 , B) $\rho_{DM0}=500$ GeV/cm^3 .

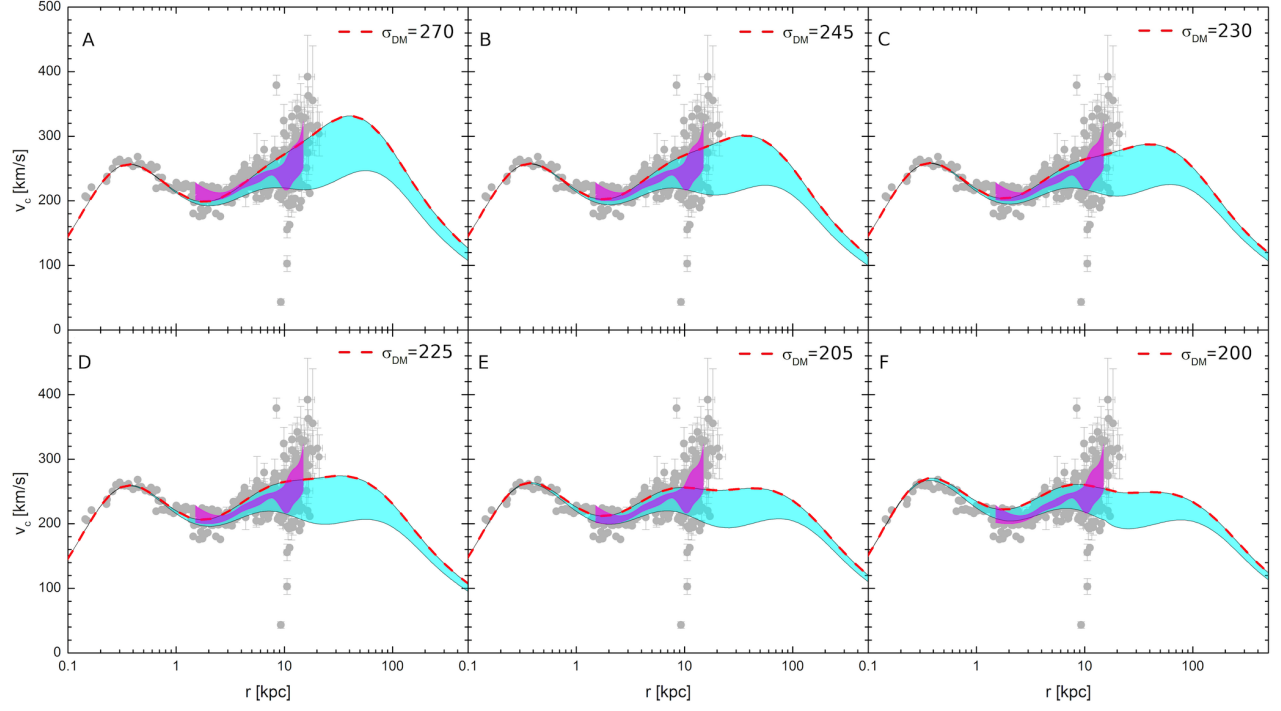


FIG. 17: The rotation curves for the range of dark matter models allowed by the constraint $v_c(R_\odot) = 220 - 260$ km/s are shown in blue for the disk model where $\Sigma_{d,\odot} = 70$ M_\odot/pc^2 . The dashed line shows the maximum likelihood model for each choice of ρ_{DM0} (shown in bold in Table II): A) $\rho_{DM0} = 25$ GeV/cm^3 , B) $\rho_{DM0} = 50$ GeV/cm^3 , C) $\rho_{DM0} = 75$ GeV/cm^3 , D) $\rho_{DM0} = 100$ GeV/cm^3 , E) $\rho_{DM0} = 250$ GeV/cm^3 , F) $\rho_{DM0} = 500$ GeV/cm^3 .

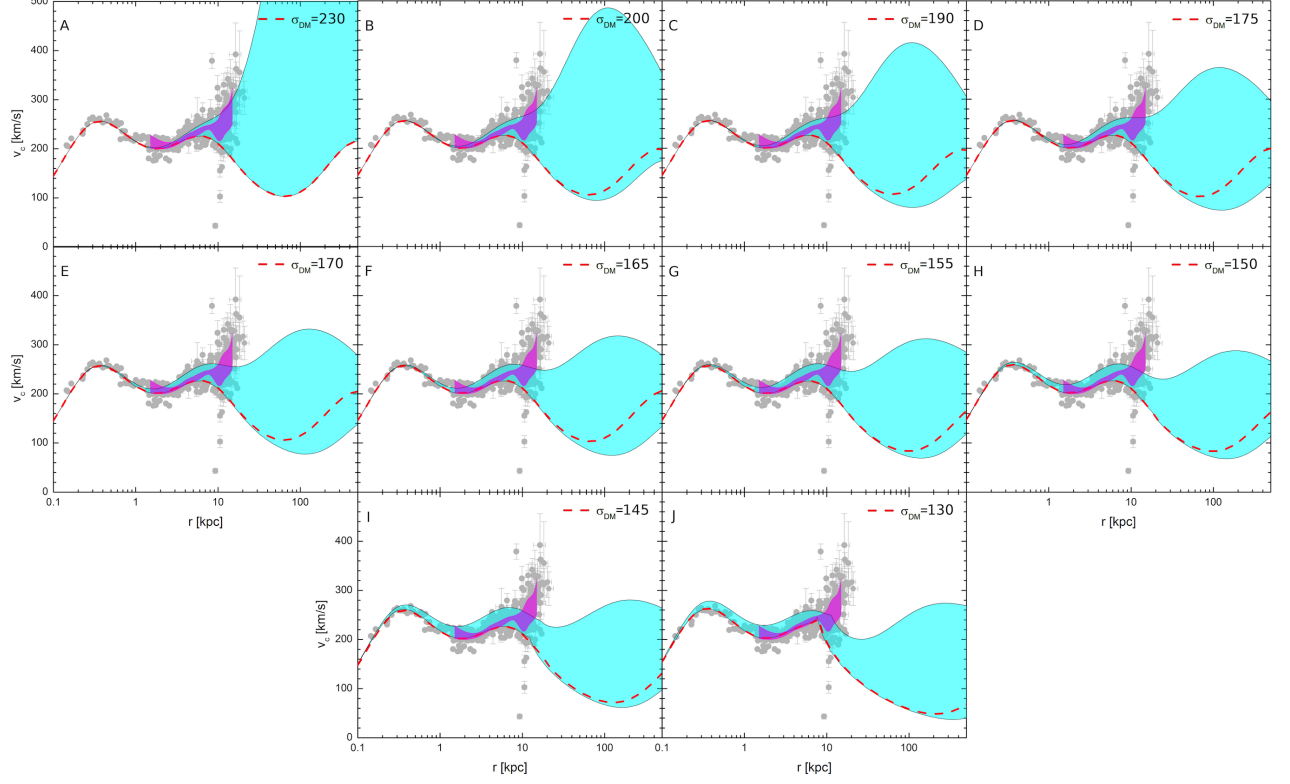


FIG. 18: The rotation curves for the range of dark matter models allowed by the constraint $v_c(R_\odot) = 220 - 260$ km/s are shown in blue for the heaviest disk model where $\Sigma_{d,\odot} = 100$ M_\odot/pc^2 . The dashed line shows the maximum likelihood model for each choice of ρ_{DM0} (shown in bold in Table III): A) $\rho_{DM0} = 1$ GeV/cm^3 , B) $\rho_{DM0} = 5$ GeV/cm^3 , C) $\rho_{DM0} = 10$ GeV/cm^3 , D) $\rho_{DM0} = 25$ GeV/cm^3 , E) $\rho_{DM0} = 50$ GeV/cm^3 , F) $\rho_{DM0} = 75$ GeV/cm^3 , G) $\rho_{DM0} = 100$ GeV/cm^3 , H) $\rho_{DM0} = 250$ GeV/cm^3 , I) $\rho_{DM0} = 500$ GeV/cm^3 , J) $\rho_{DM0} = 1000$ GeV/cm^3 .

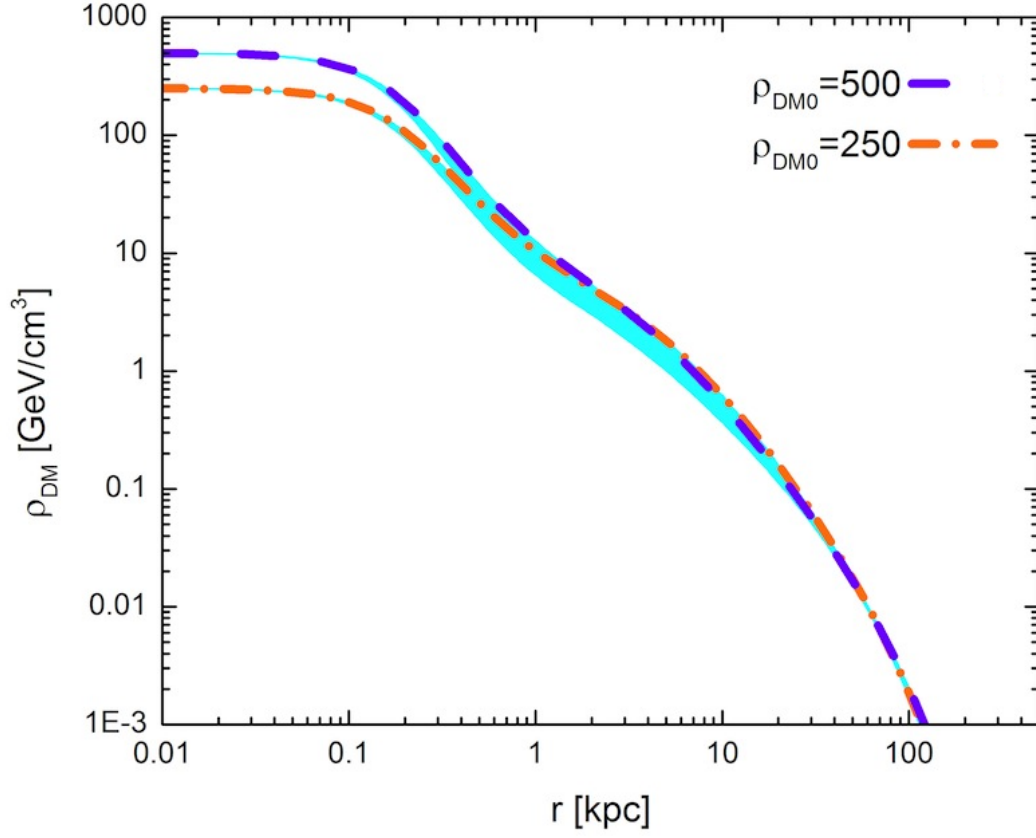


FIG. 19: The range of radial dark matter density profiles for the $\Sigma_{d,\odot}=40 \text{ M}_\odot/\text{pc}^2$ disk are plotted in blue for the dark matter models allowed by $v_c(R_\odot) = 220 - 260 \text{ km/s}$. The bold lines indicate the best fit models corresponding to the allowed values of $\rho_{\text{DM}0}$ (shown in bold in Table I).

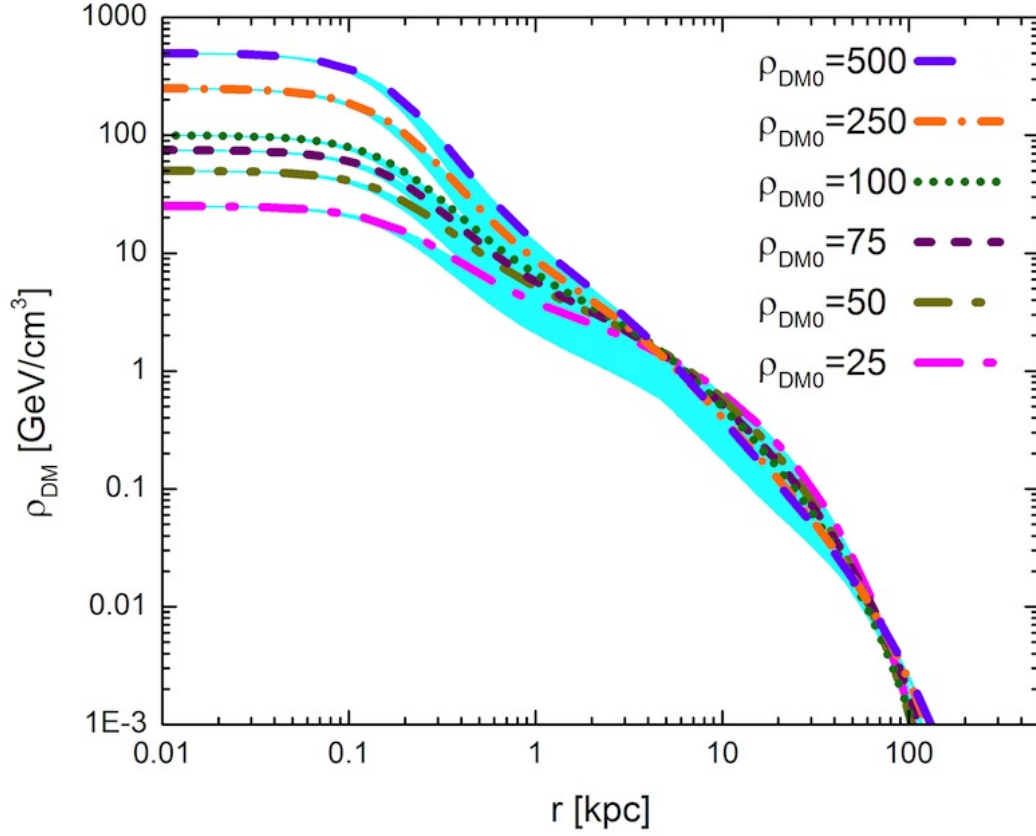


FIG. 20: The range of radial dark matter density profiles for the $\Sigma_{d,\text{odot}}=70 \text{ M}_{\odot}/\text{pc}^2$ disk are plotted in blue for the dark matter models allowed by $v_c(R_{\odot}) = 220 - 260 \text{ km/s}$. The bold lines indicate the best fit models corresponding to the allowed values of $\rho_{\text{DM}0}$ (shown in bold in Table II).

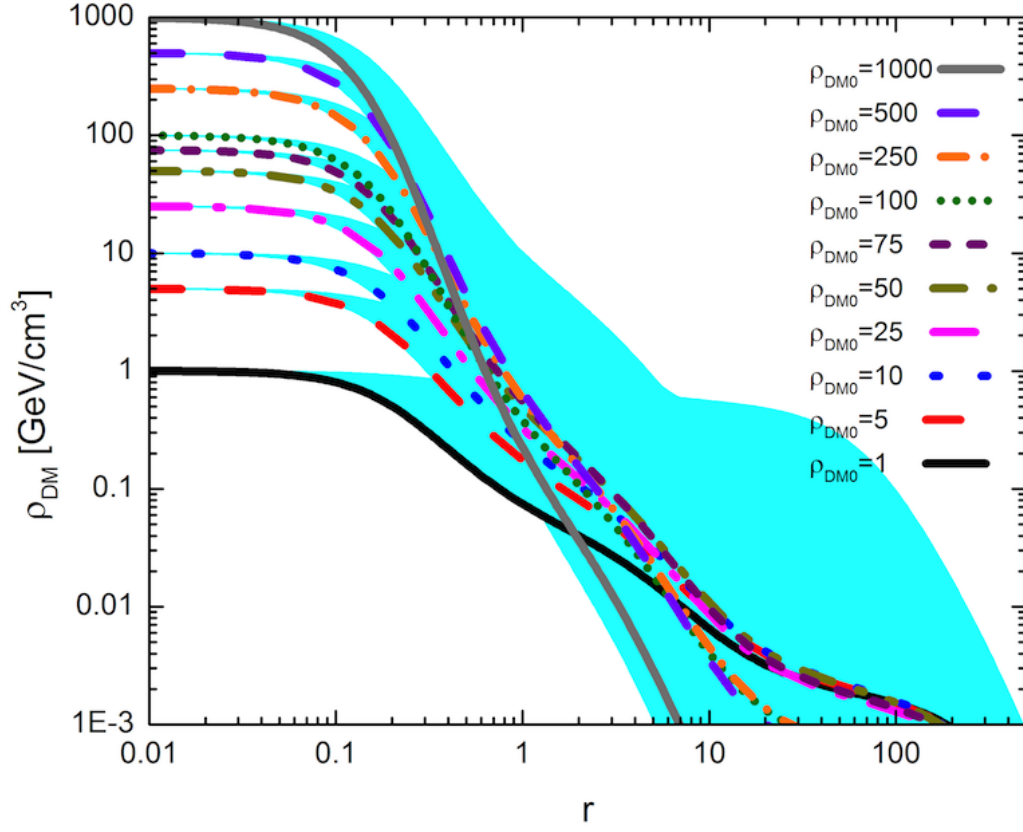


FIG. 21: The range of radial dark matter density profiles for the $\Sigma_{d,\odot}=100 \text{ M}_\odot/\text{pc}^2$ disk are plotted in blue for the dark matter models allowed by $v_c(R_\odot) = 220 - 260 \text{ km/s}$. The bold lines indicate the best fit models corresponding to the allowed values of $\rho_{\text{DM}0}$ (shown in bold in Table II).

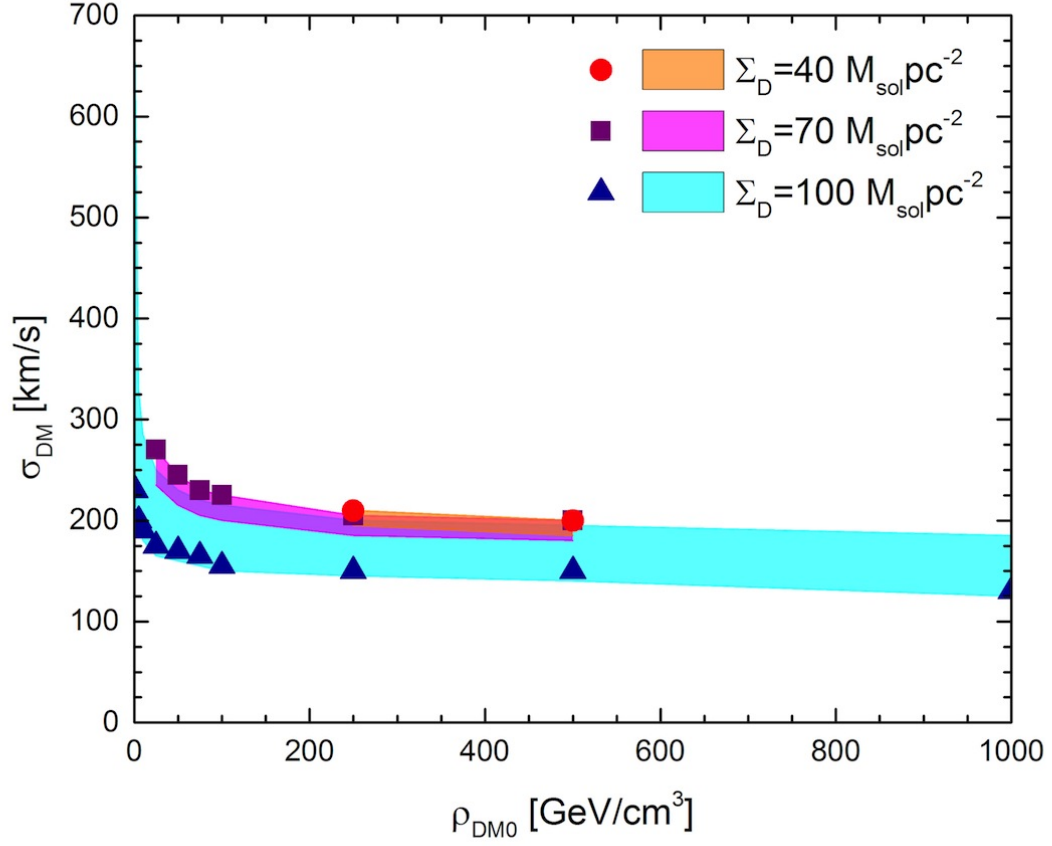


FIG. 22: The allowed σ_{DM} (as defined in eq. 13) constrained by the rotation curve is shown for each of the three disk models by colored bands. The points represent the most probable models for each ρ_{DM0} as determined by the BHB/BS analysis.

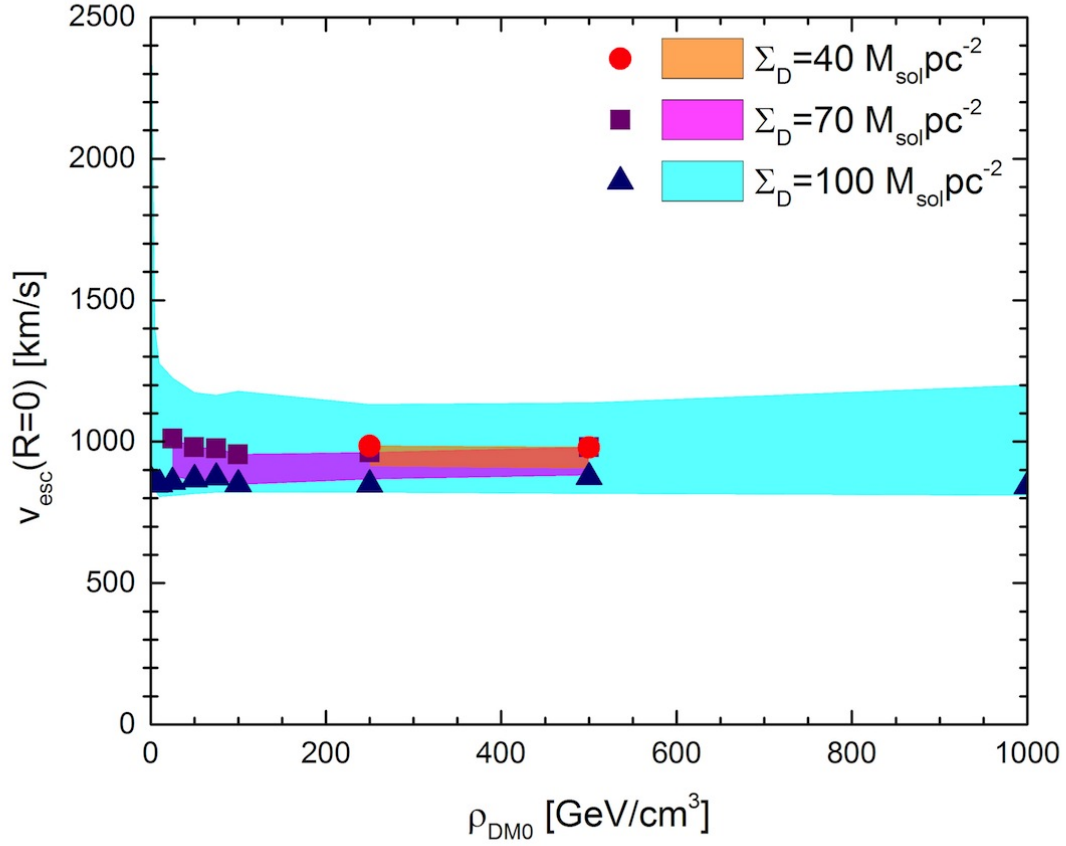


FIG. 23: The allowed escape velocity from the center of the Galaxy constrained by the rotation curve is plotted for each of the three disk models as a function of the central dark matter density as colored bands. The points represent the most probable $v_{esc}(R=0)$ for each ρ_{DM0} as determined by the BHB/BS analysis.

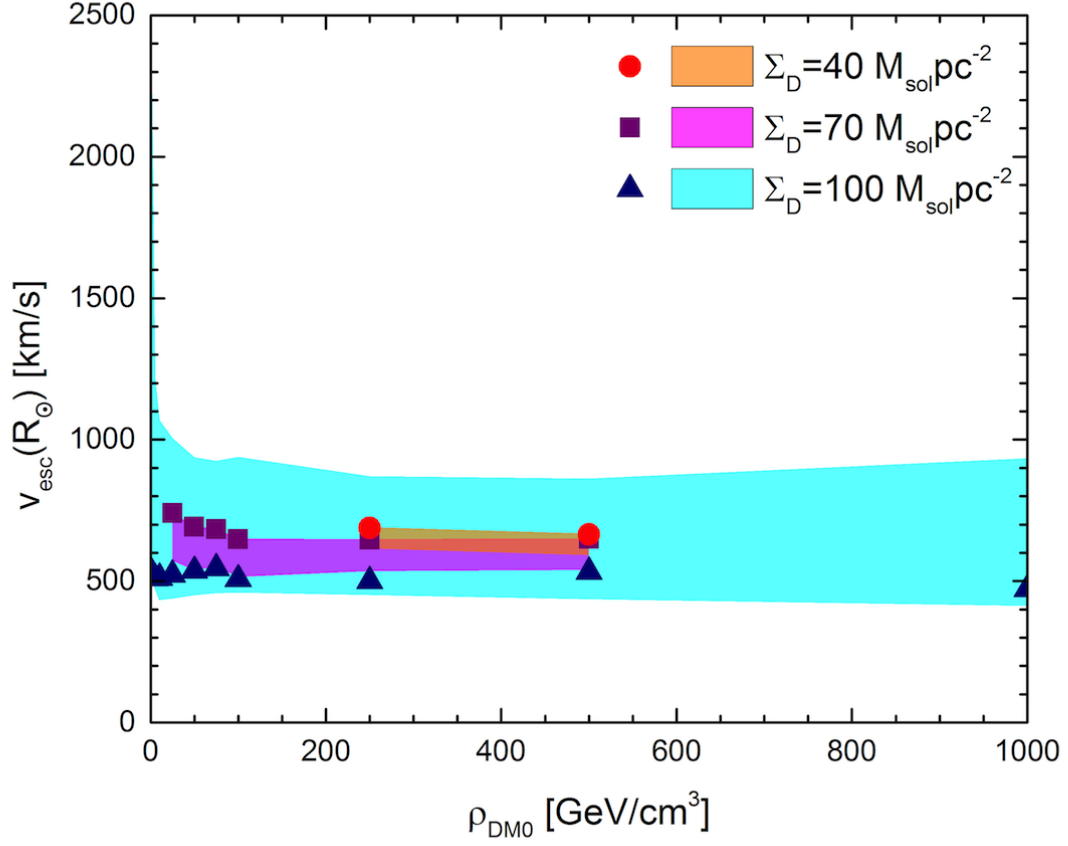


FIG. 24: The allowed local escape velocity constrained by the rotation curve is plotted for each of the three disk models as a function of the central dark matter density. The points represent the most probable $v_{\text{esc}}(R_{\odot})$ for each $\rho_{\text{DM}0}$ as determined by the BHB/BS analysis.

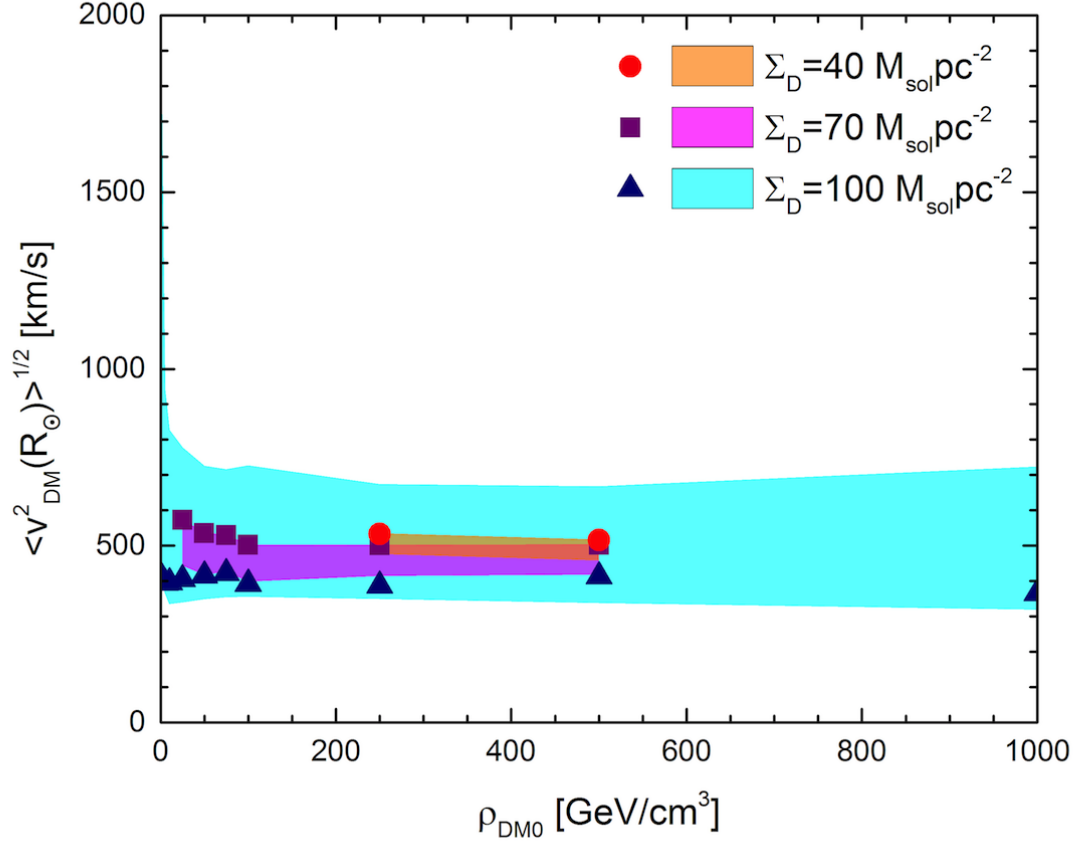


FIG. 25: The allowed local root-mean-squared constrained by the rotation curve is plotted for each of the three disk models as a function of the central dark matter density. The points represent the most probable $\langle v_{DM}^2(R_{\odot}) \rangle^{1/2}$ for each ρ_{DM0} as determined by the BHB/BS analysis.

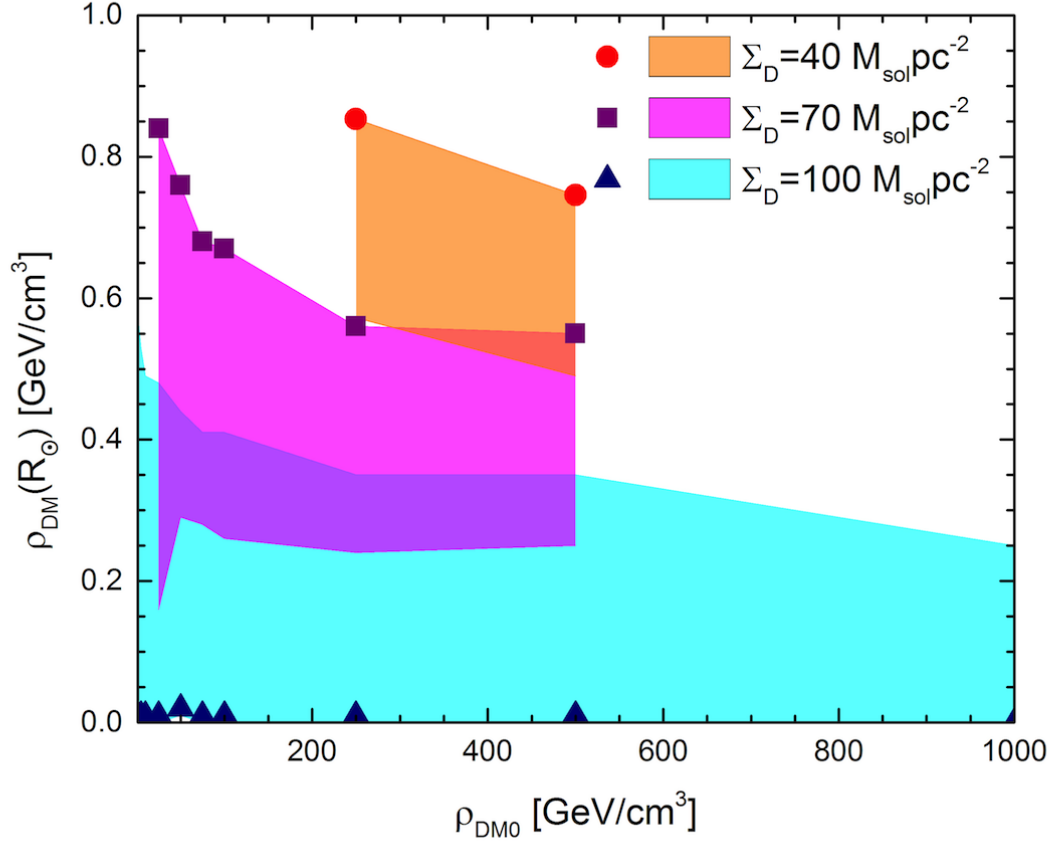


FIG. 26: The allowed local dark matter density constrained by the rotation curve is plotted for each of the three disk models as a function of the central dark matter density. The points represent the most probable $\rho_{DM}(R_\odot)$ for each ρ_{DM0} as determined by the BHB/BS analysis.

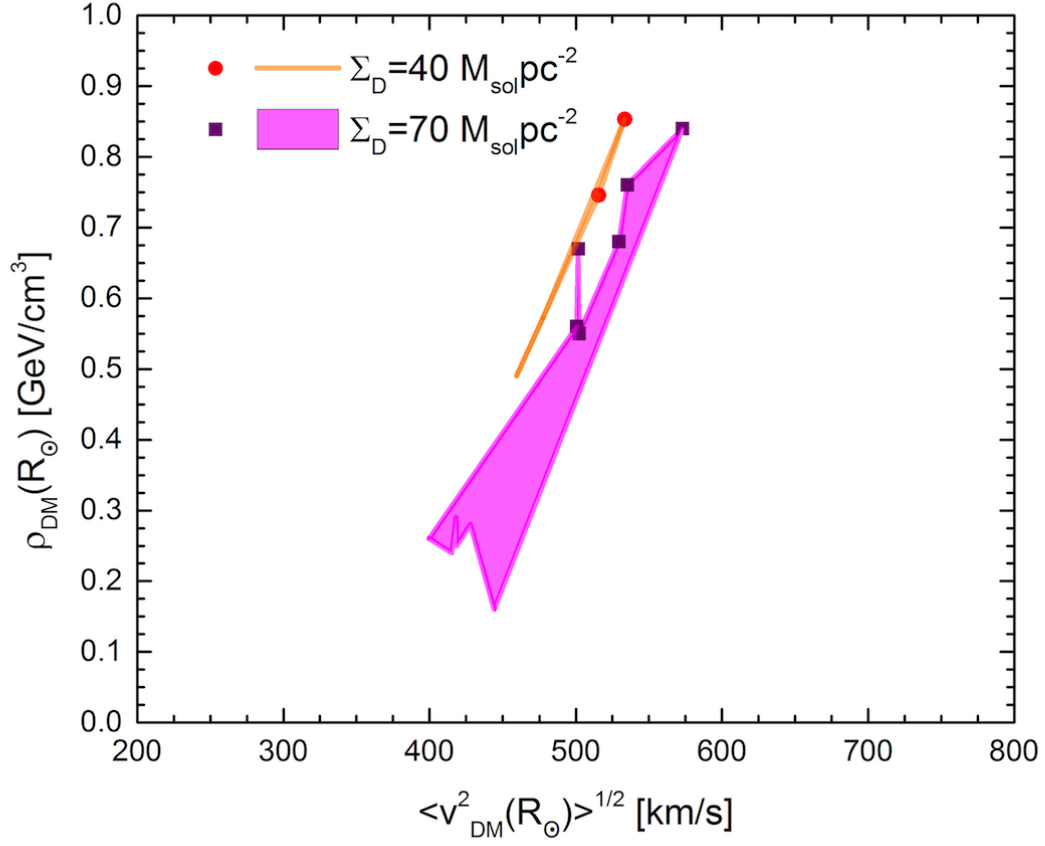


FIG. 27: The allowed local dark matter density constrained by the rotation curve is plotted for the $\Sigma_{d,\odot}=40 \text{ M}_\odot/\text{pc}^2$ and $\Sigma_{d,\odot}=70 \text{ M}_\odot/\text{pc}^2$ models. The points represent the most probable $\rho_{DM}(R_\odot)$ as a function of $\langle v_{DM}^2(R_\odot) \rangle^{1/2}$ as determined by the BHB/BS analysis.

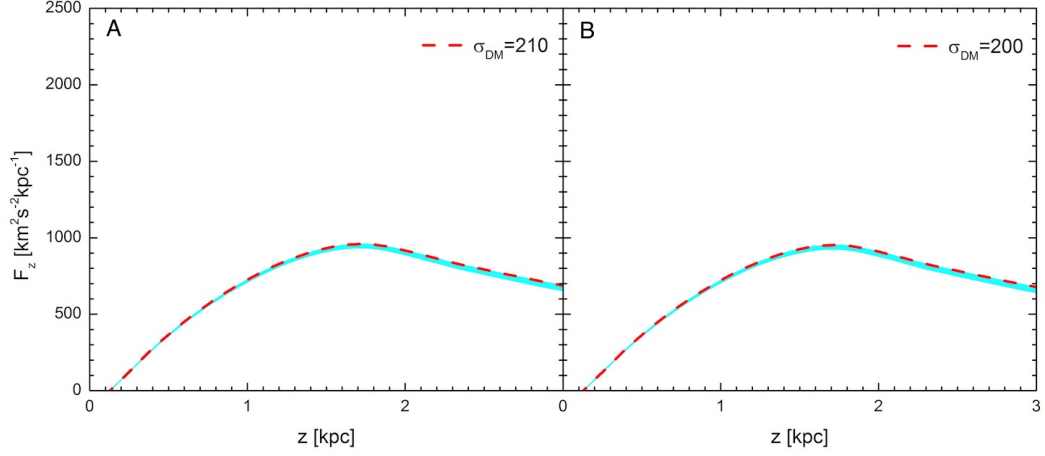


FIG. 28: The range of vertical force profiles at R_\odot for the $\Sigma_{d,\odot}=40 \text{ M}_\odot/\text{pc}^2$ disk are shown in blue for the dark matter models allowed by $v_c(R_\odot) = 220 - 260 \text{ km/s}$. The dashed line shows the maximum likelihood model for each choice of ρ_{DM0} (shown in bold in Table I): A) $\rho_{DM0}=250 \text{ GeV/cm}^3$, B) $\rho_{DM0}=500 \text{ GeV/cm}^3$.

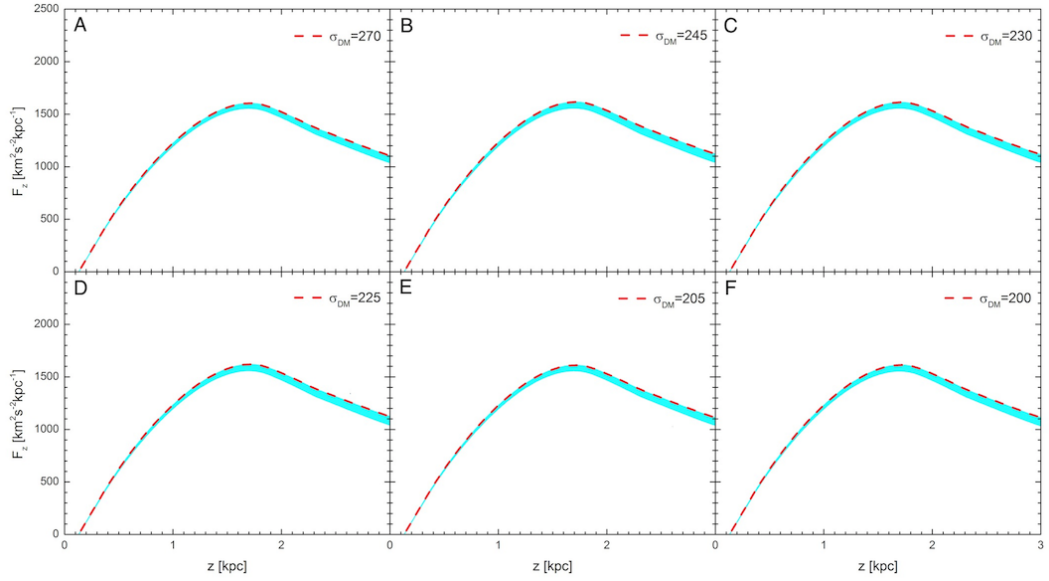


FIG. 29: The range of vertical force profiles at R_\odot for the $\Sigma_{d,\odot}=70 \text{ M}_\odot/\text{pc}^2$ disk are shown in blue for the dark matter models allowed by $v_c(R_\odot) = 220 - 260 \text{ km/s}$. The dashed line shows the maximum likelihood model for each choice of ρ_{DM0} (shown in bold in Table II): A) $\rho_{DM0}=25 \text{ GeV/cm}^3$, B) $\rho_{DM0}=50 \text{ GeV/cm}^3$, C) $\rho_{DM0}=75 \text{ GeV/cm}^3$, D) $\rho_{DM0}=100 \text{ GeV/cm}^3$, E) $\rho_{DM0}=250 \text{ GeV/cm}^3$, F) $\rho_{DM0}=500 \text{ GeV/cm}^3$.

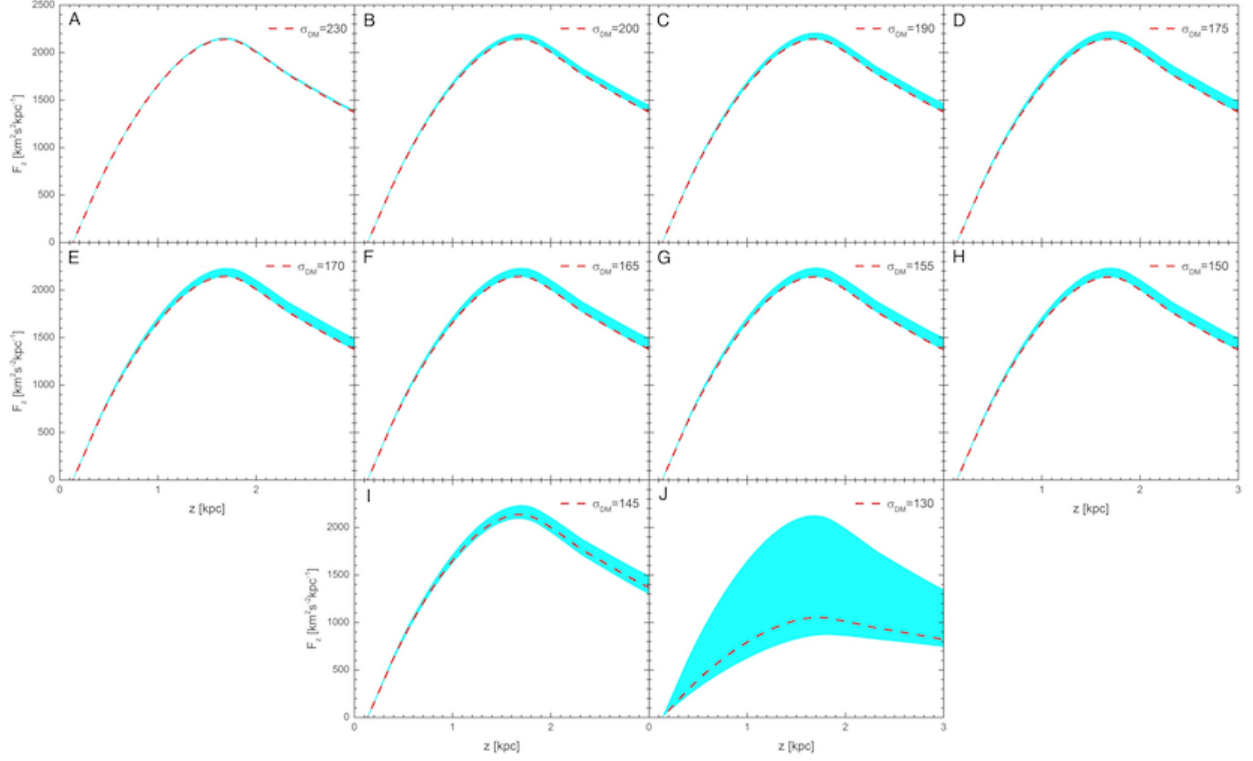


FIG. 30: The range of vertical force profiles at R_\odot for the $\Sigma_{d,\odot}=100 \text{ M}_\odot/\text{pc}^2$ disk are shown in blue for the dark matter models allowed by $v_c(R_\odot) = 220 - 260 \text{ km/s}$. The dashed line shows the maximum likelihood model for each choice of ρ_{DM0} (shown in bold in Table III): A) $\rho_{DM0}=1 \text{ GeV/cm}^3$, B) $\rho_{DM0}=5 \text{ GeV/cm}^3$, C) $\rho_{DM0}=10 \text{ GeV/cm}^3$, D) $\rho_{DM0}=25 \text{ GeV/cm}^3$, E) $\rho_{DM0}=50 \text{ GeV/cm}^3$, F) $\rho_{DM0}=75 \text{ GeV/cm}^3$, G) $\rho_{DM0}=100 \text{ GeV/cm}^3$, H) $\rho_{DM0}=250 \text{ GeV/cm}^3$, I) $\rho_{DM0}=500 \text{ GeV/cm}^3$, J) $\rho_{DM0}=1000 \text{ GeV/cm}^3$.

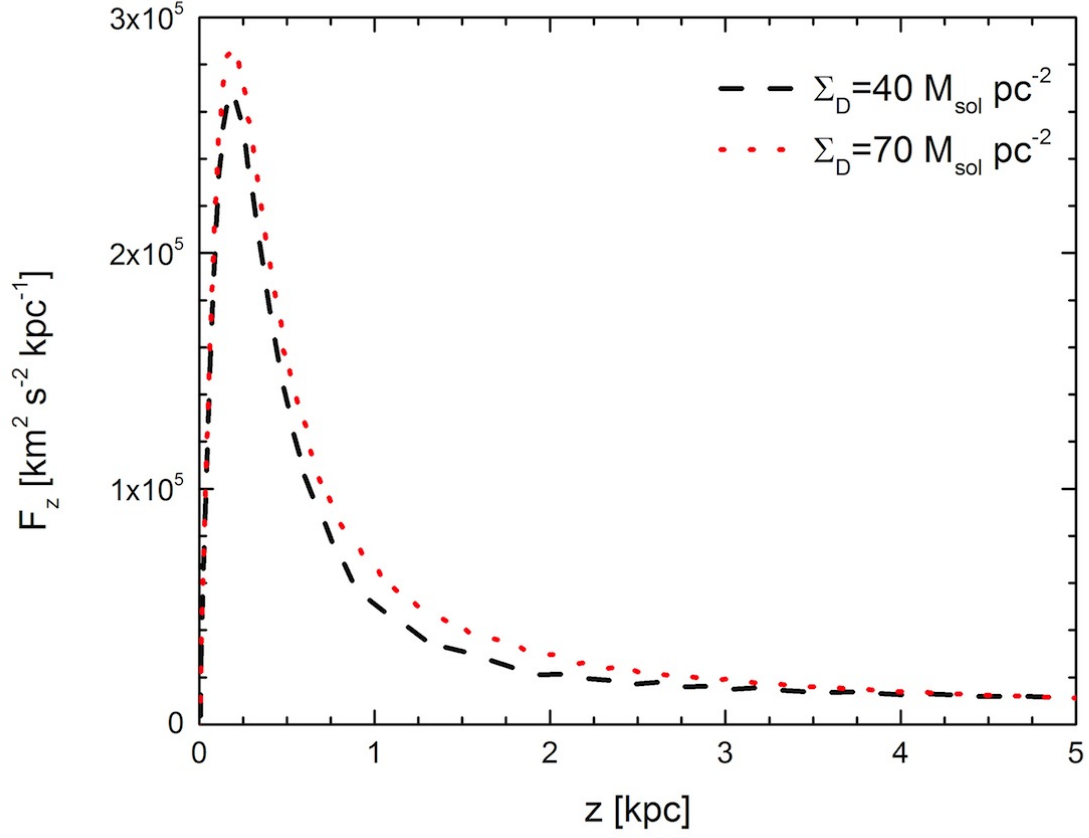


FIG. 31: The vertical force profile at the Galactic center is shown for the $\Sigma_{d,\odot}=40 \text{ M}_{\odot}/\text{pc}^2$ and $\Sigma_{d,\odot}=70 \text{ M}_{\odot}/\text{pc}^2$ models where $\rho_{DM0} = 500 \text{ GeV}/\text{cm}^3$ and $\sigma_{DM} = 200 \text{ km/s}$. These are the most probable models for the corresponding disk surface densities based on the BHB/BS analysis.

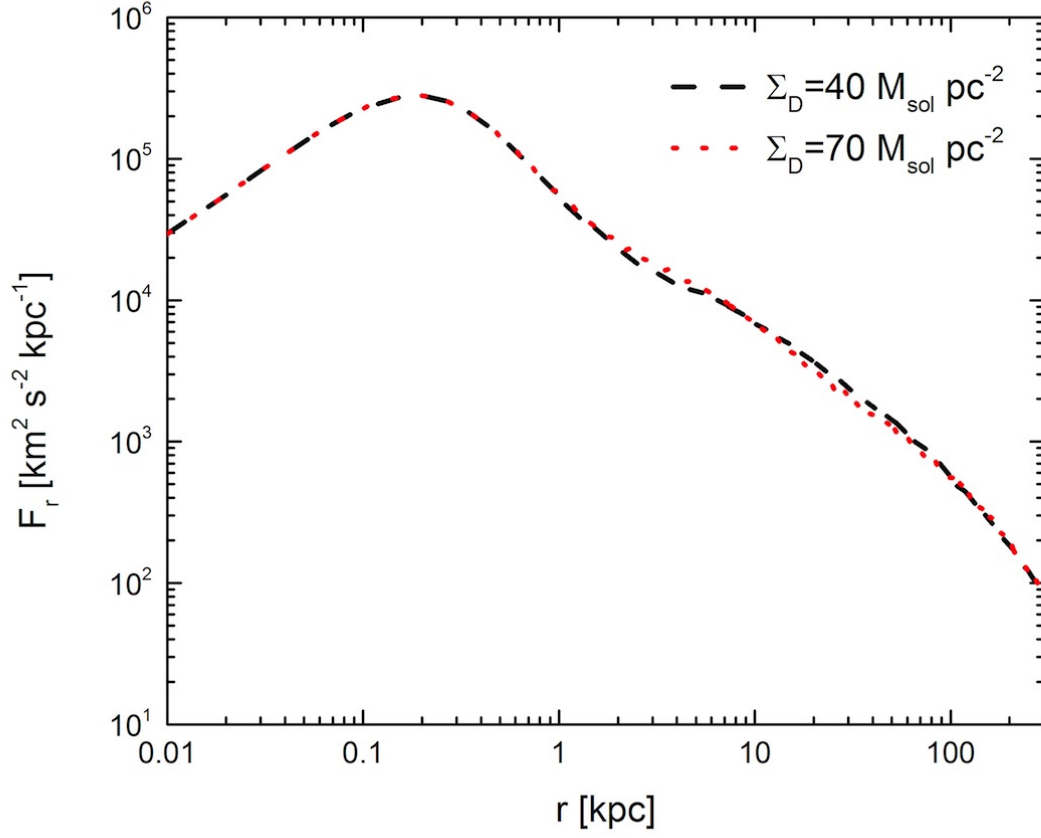


FIG. 32: The radial force profile in the Galactic plane ($z = 0$) is shown for the $\Sigma_{d,\odot}=40$ M_{\odot}/pc^2 and $\Sigma_{d,\odot}=70$ M_{\odot}/pc^2 models where $\rho_{DM0} = 500$ GeV/cm^3 and $\sigma_{DM} = 200$ km/s . These are the most probable models for the corresponding disk surface densities based on the BHB/BS analysis.

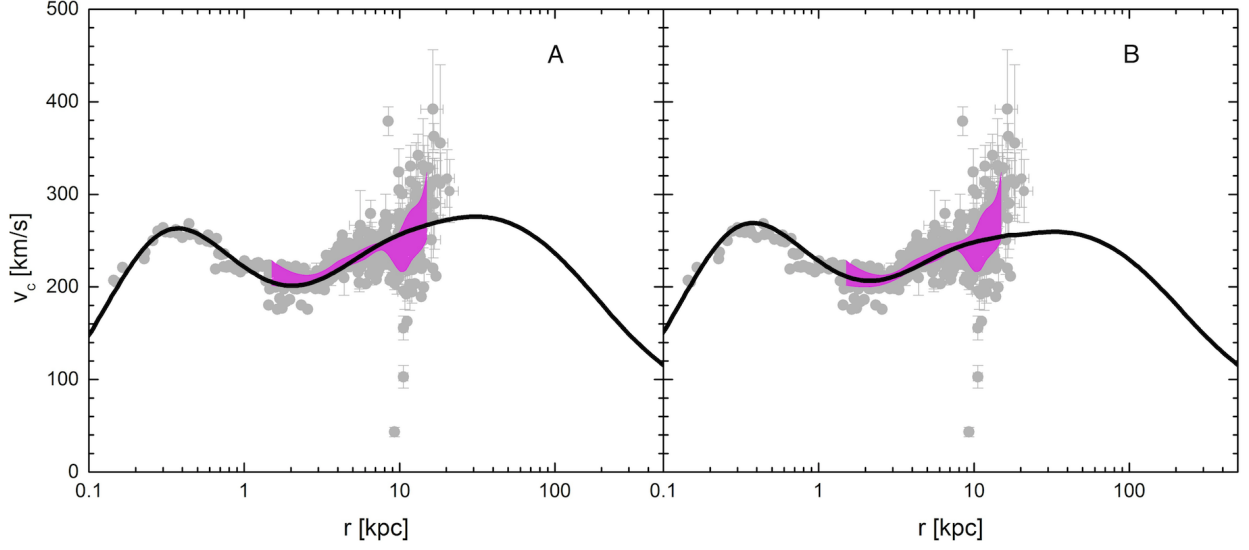


FIG. 33: The dark matter models which best fit the observations of the observations of the rotation curve are plotted for the $\Sigma_{d,\odot}=40 \text{ M}_{\odot}/\text{pc}^2$ disk. The various parameters of these models are found in Table IV. A) $\rho_{DM0}=250 \text{ GeV}/\text{cm}^3$, $\sigma_{DM}=205 \text{ km/s}$; B) $\rho_{DM0}=500 \text{ GeV}/\text{cm}^3$, $\sigma_{DM}=195 \text{ km/s}$

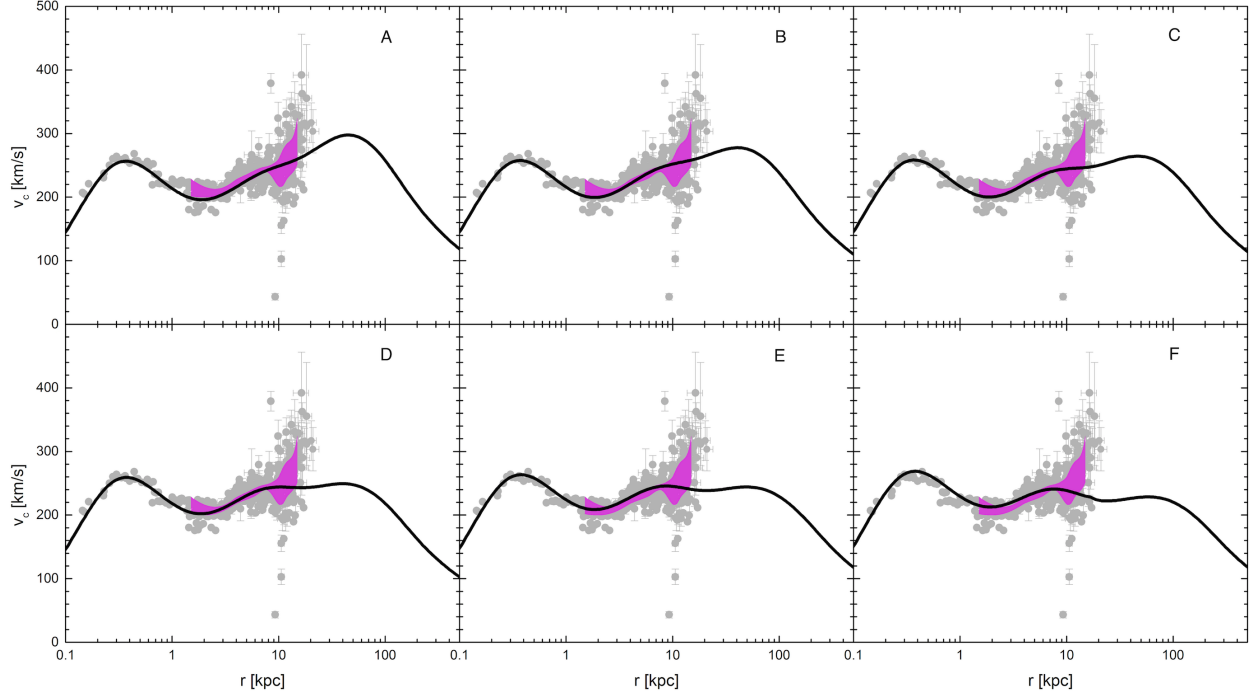


FIG. 34: The dark matter models which best fit the observations of the rotation curve are plotted for the $\Sigma_{d,\odot}=70 \text{ M}_\odot/\text{pc}^2$ disk. The various parameters of these models are found in Table IV. A) $\rho_{DM0}=25 \text{ GeV}/\text{cm}^3$, $\sigma_{DM}=255 \text{ km/s}$; B) $\rho_{DM0}=50 \text{ GeV}/\text{cm}^3$, $\sigma_{DM}=235 \text{ km/s}$; C) $\rho_{DM0}=75 \text{ GeV}/\text{cm}^3$, $\sigma_{DM}=220 \text{ km/s}$; D) $\rho_{DM0}=100 \text{ GeV}/\text{cm}^3$, $\sigma_{DM}=215 \text{ km/s}$; E) $\rho_{DM0}=250 \text{ GeV}/\text{cm}^3$, $\sigma_{DM}=200 \text{ km/s}$; F) $\rho_{DM0}=500 \text{ GeV}/\text{cm}^3$, $\sigma_{DM}=195 \text{ km/s}$

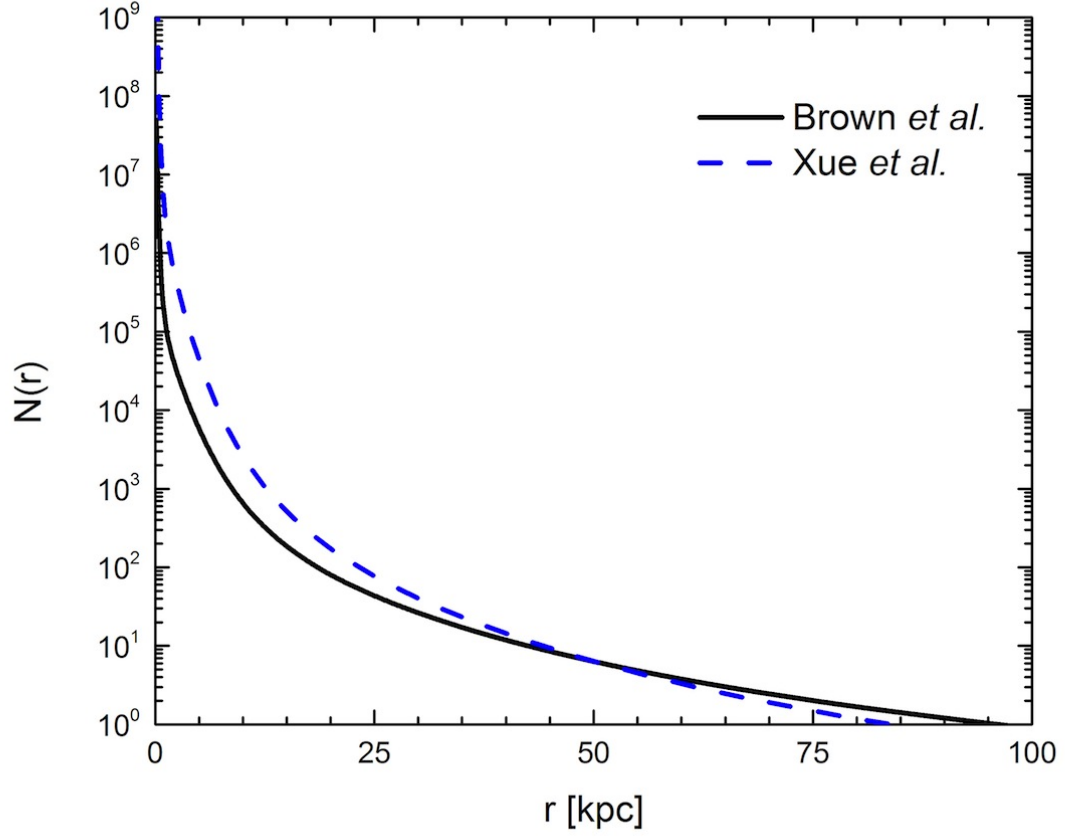


FIG. 35: The distribution of BHB and BS stars expected from the velocity distribution measured by Brown *et al.* and Xue *et al.* The distribution is shown for the $\Sigma_{d,\odot}=70$ M_{\odot}/pc^2 disk with $\rho_{DM0} = 500 \text{ GeV}/\text{cm}^3$, $\sigma_{DM} = 200 \text{ km/s}$, and $\sigma_{BHB} = \sigma_{BS} = 115 \text{ km/s}$ for Brown *et al.* and $\sigma_{BHB} = 106 \text{ km/s}$ for Xue *et al.*